NRL Memorandum Report 3416

DARPA-NRL Laser Program

Semiannual Technical Report to Defense Advanced Research Projects Agency 1 January 1976 - 30 June 1976

Laser Physics Branch
Optical Sciences Division

November 1976

NAVAL RESEARCH LABORATORY
Washington, D.C.

SECURITY CLASSIFICATION OF THIS PAGE (When Data Entered)

REPORT DOCUMENTATION PAGE

READ INSTRUCTIONS BEFORE COMPLETING FORM

1. REPORT NUMBER: NRL ~~Memorandum Report~~ MR-3416
2. GOVT ACCESSION NO.
3. RECIPIENT'S CATALOG NUMBER

4. TITLE (and Subtitle): DARPA-NRL LASER PROGRAM — SEMIANNUAL TECHNICAL REPORT TO DEFENSE ADVANCED RESEARCH PROJECTS AGENCY — 1 January 1976 - 30 June 1976

5. TYPE OF REPORT & PERIOD COVERED: Interim report [illegible]

6. PERFORMING ORG. REPORT NUMBER

7. AUTHOR(s): J.R. Airey, R. Burnham, L. Champagne, N. Djeu, J. Eversole

8. CONTRACT OR GRANT NUMBER(s): DARPA Order-2062

9. PERFORMING ORGANIZATION NAME AND ADDRESS
Naval Research Laboratory
Washington, D.C. 20375

10. PROGRAM ELEMENT, PROJECT, TASK AREA & WORK UNIT NUMBERS
NRL Problem K03-53
Project 5E20

11. CONTROLLING OFFICE NAME AND ADDRESS
Defense Advanced Research Projects Agency
Arlington, Virginia 22209

12. REPORT DATE: November 1976

13. NUMBER OF PAGES: 96 (12) 96p.

14. MONITORING AGENCY NAME & ADDRESS(if different from Controlling Office)

15. SECURITY CLASS. (of this report): UNCLASSIFIED

15a. DECLASSIFICATION/DOWNGRADING SCHEDULE

16. DISTRIBUTION STATEMENT (of this Report)

Approved for public release; distribution unlimited.

17. DISTRIBUTION STATEMENT (of the abstract entered in Block 20, if different from Report)

18. SUPPLEMENTARY NOTES

19. KEY WORDS (Continue on reverse side if necessary and identify by block number)

Lasers
Electrical lasers
Chemical lasers
Laser diagnostics
Electronic state lasers
Chemical kinetics
Electronic state lifetimes
Energy transfer
Chemiluminescence

20. ABSTRACT (Continue on reverse side if necessary and identify by block number)

The DARPA-NRL Laser Program is concerned with the development of laser technology with the emphasis on electronic state lasers and the associated physics. Electrically excited infrared lasers and intramolecular energy transfer are also being studied.

Progress is reported in all areas with the major highlights being (i) the observation of quasi-CW lasing in XeF (ii) the discovery of the KrCl laser at 223 nm (iii) advancement of discharge-pumped rare-gas halide lasers and their understanding, and (iv) improvements in the performance of the CO-C_2H_2 and CO-CS_2 energy transfer lasers which are being studied in the electric-discharge gasdynamic laser facility.

DD FORM 1 JAN 73 1473 EDITION OF 1 NOV 65 IS OBSOLETE S/N 0102-014-6601

251 950

SECURITY CLASSIFICATION OF THIS PAGE (When Data Entered)

bpg

TABLE OF CONTENTS

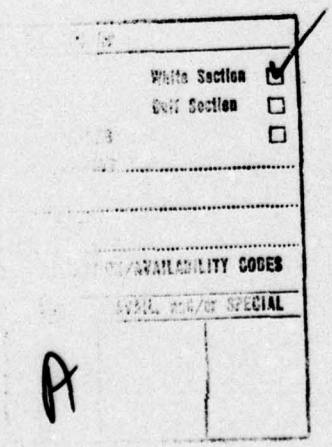

FOREWORD

The Laser Physics Branch of the Optical Sciences Division, Naval Research Laboratory, Washington, D. C., prepared this semiannual report on work sponsored by the Defense Advanced Research Projects Agency, DARPA Order 2062. The projects described are also funded by NRL-ONR research funds. Co-authors of the report were J. R. Airey, R. Burnham, L. Champagne, N. Djeu, J. Eversole, J. G. Eden, D. Frankel, N. W. Harris, S. K. Searles, J. A. Stregack, W. S. Watt, and B. Wexler.

SEMIANNUAL TECHNICAL REPORT

REPORTING PERIOD

1 January 1976 - 30 June 1976

1.	DARPA Order	2062, Amendment No. 5
2.	Program Code Number	5E20
3.	Name of Contractor	Naval Research Laboratory
4.	Effective Date of Contract	1 July 1972
5.	Contract Expiration Date	30 June 1976
6.	Amount of Contract	$550,000
7.	Contract Number	62301E
8.	Principal Investigator	J. R. Airey
9.	Telephone Number	(202) 767-3217
10.	Project Scientist	W. S. Watt
11.	Telephone Number	(202) 767-2074
12.	Title of Work	DARPA/NRL Laser Technology Program

SPONSORED BY

DEFENSE ADVANCED RESEARCH PROJECTS AGENCY

DARPA Order No. 2062

DARPA-NRL LASER PROGRAM

Semiannual Technical Report to Defense Advanced Research Projects Agency
1 January 1976 - 30 June 1976

CHEMICAL INFRARED LASERS

1. Maxwell Cold-Cathode Electron Beam Controlled System

The objective during this reporting period was to implement modifications to the cold cathode electron beam system which were outlined in the previous report.[1] The major tasks were to redesign the discharge chamber and to upgrade the gas handling system in order to handle toxic and corrosive chemical compounds. These have been completed and a series of measurements have been performed which characterize the operation of the system. Measurements were made both with and without gas in the discharge chamber. Nitrogen was chosen for these diagnostic experiments, since its transport properties are well known.

As a result of a change in DARPA program priorities, further pulsed HCl-chemical laser studies were not pursued. Instead, preliminary experiments were performed using a one microsecond current pulse to initiate laser action in the rare gas monohalide-xenon fluoride (XeF). Stimulated emission was observed and lasing pulses comparable in length to the initiating current pulse have been observed.

Experimental Apparatus

The objective in modifying the Maxwell electron-beam controlled system (Fig. 1) was to be able to safely store,

Note: Manuscript submitted November 10, 1976.

transport, and work with toxic and corrosive chemicals. A gas handling system was designed and built which included facilities to mix and store a wide variety of toxic chemicals. The mixing and gas handling system as well as the discharge chamber are constructed entirely of corrosion resistant "Monel"[2] and Teflon[3] components. This gas handling system can be operated to 300 psia and the laser chamber can be operated to 90 psia. The operating characteristics of the new discharge chamber are listed in Table I.

Table I

Pressure range	10^{-4} torr - 90 psia
Chamber volume	7 liters
Optical aperture	2.22 cm
Gain length	1 meter
Active laser volume	387 cm^3
E-beam foil aperture	325 cm^2

Figure 2 is a view of the discharge chamber in cross section. The electron beam current monitor which is housed within the adaptor plate measures the electron beam current (I_b) which is incident to the foil. The sustainer bank can be charged to and diverted at any voltage up to 75 kV.

Discharge Characteristics

Figure 3 shows the current density (J_b) and charge density ($J_b \cdot t_p$) which is incident to the foil (25 μm

Titanium) at various gun to foil spacings. This measurement is obtained from the beam-current monitor. The maximum value of J_b and $(J_b \cdot t_p)$ is limited by the gap closure (or by arc formation time). Gap closure occurs at a rate between 2 cm/μsec and 4 cm/μsec with the probability of an arc occurring at 4 cm/μsec being very low (~ 1%). By fitting the laser chamber with a special anode which contains a current density button[4] it was possible to measure the current density (J_b) and charge density ($J_b \cdot t_p$) which was transmitted through the foil into the active volume of the discharge chamber (Fig. 4). The measured value of the beam current density transmitted into the evacuated discharge chamber (10^{-4} torr) was in good agreement with similar measurements which were performed using a Faraday cup.[1] Figure 4 shows the current density which is incident upon the active volume. This current is due solely to the primary electron beam. From Figs. 3 and 4 we see that approximately 50% of the current which is incident to the foil reaches the region of interest.

In subsequent experiments, the current density in a sustained discharge (J_s) was measured. For this measurement ultra-high purity nitrogen was used because its transport properties are known.[4] Figure 5 shows the current density as a function of pressure when the Townsend Parameter (E/N) in the discharge region is kept constant. This value of

E/N ($\sim 1.1 \times 10^{-16}$ V-cm^2) was chosen to avoid any marked change in the N_4^+ recombination coefficient.[1] The N_4^+ recombination rate study of Douglas-Hamilton indicates that this rate is only weakly dependent on E/N for E/N values greater than 0.8×10^{-16} V-cm^2.

Experimental results taken with the ultra-high purity nitrogen and measured with the current density button indicate that $J_s \sim P^{3/4}$. The predicted current density behavior is closer to $J_s \sim P^{1/2}$. From these results we infer a constant correction factor which can be applied to the current density (J_s) value which is measured by the sustainer anode in the region from 0.2 to 2.0 atmospheres. At pressures above 2.0 atmospheres J_s approaches the expected $P^{1/2}$ behavior.

Following check-out of the modified system, preliminary experiments were performed to examine long-pulse cold-cathode e-beam excitation of rare gas monohalides. Stimulated emission was observed in XeF with quasi-CW laser pulses, shown in Fig. 6, obtained from gas mixtures of Ar: Xe:NF_3 at 2.5 atm pressure.[5] The significance of this discovery of long-pulse laser operation on the bound-bound XeF transition has important implications for the scaling of rare-gas halide lasers. Work is continuing to investigate and characterize quasi-continuous rare gas monohalide laser systems.

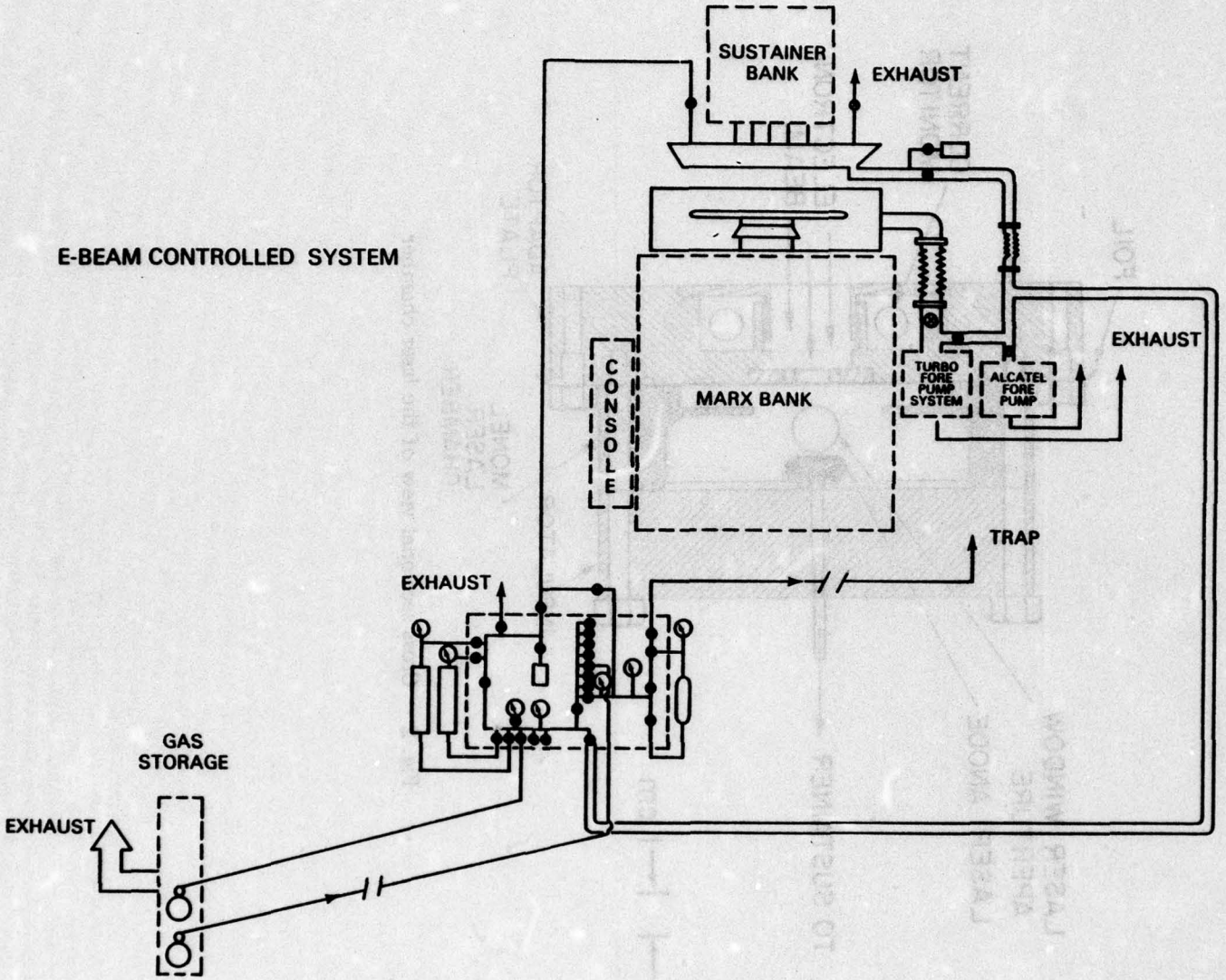

Fig. 1 — A schematic diagram of the modified laser system

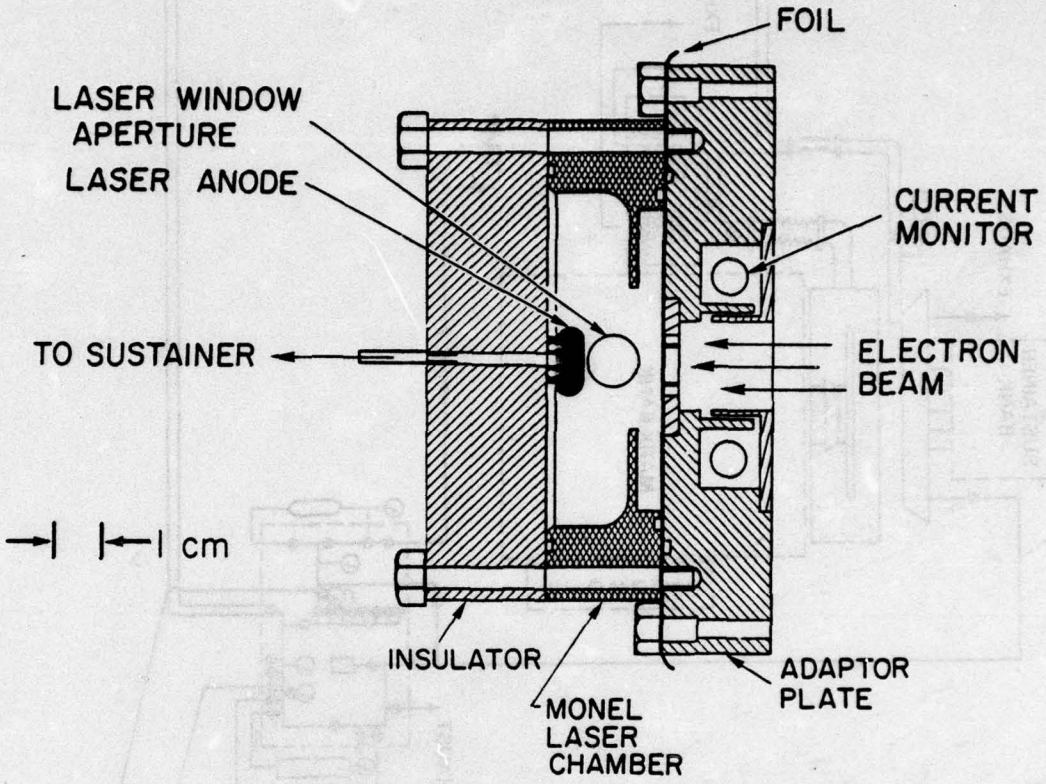

Fig. 2 — Cross sectional view of the laser chamber

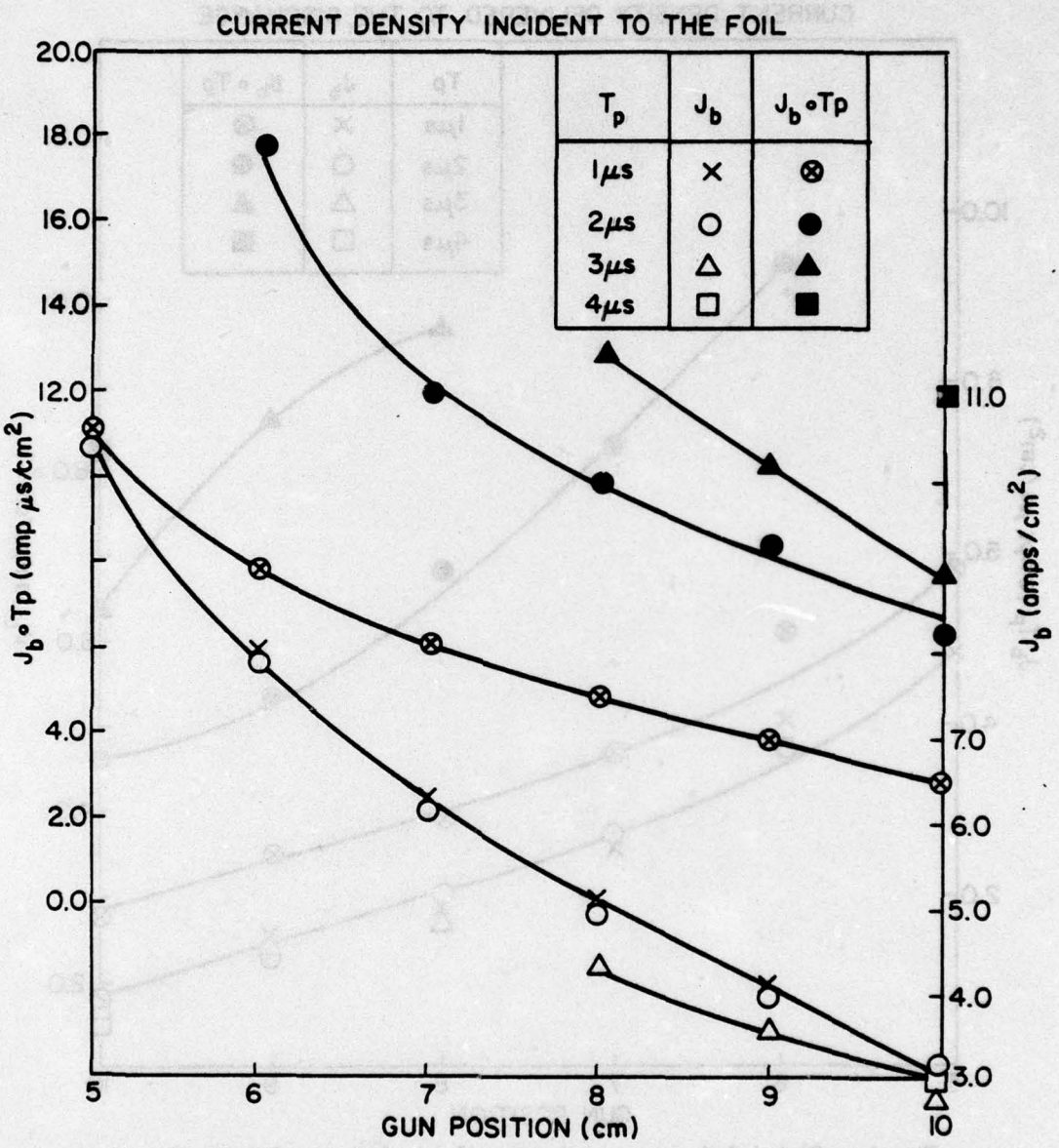

Fig. 3 — Plot of the current density J_b incident to the foil (25 μm titanium) for 1 μsec (x) 2 μsec (o) 3 μsec (△) and 4 μsec (□) pulses at a gun voltage of 300 kV. Charge density ($J_b \cdot t$) is also plotted. Measurements were made with a current density button.

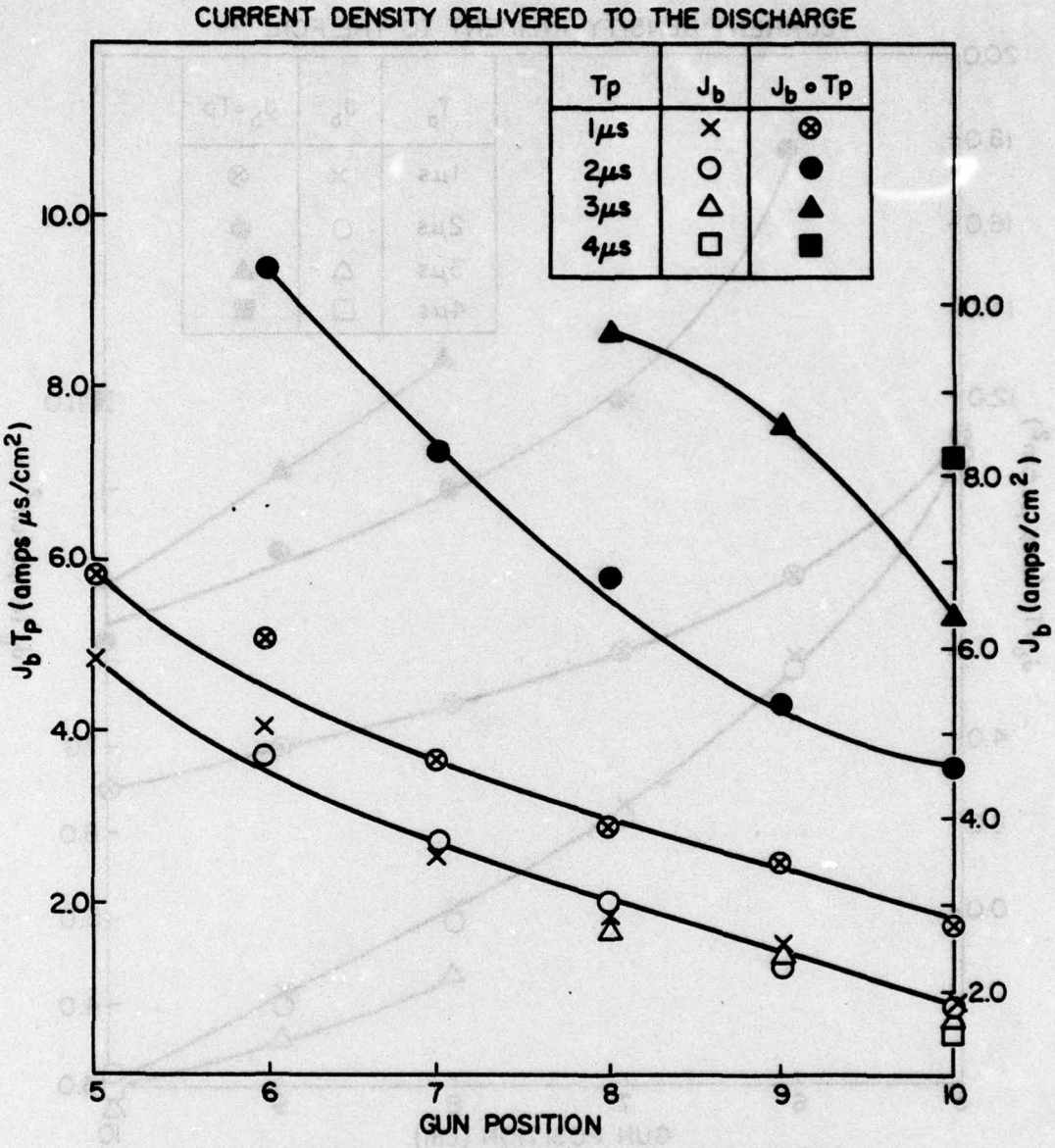

Fig. 4 — Plots of the current density (J_b) and charge density ($J_b \cdot t$) which is transmitted through the foil (25 μm titanium) and is incident to the active volume. These measurements were made with a current density button.

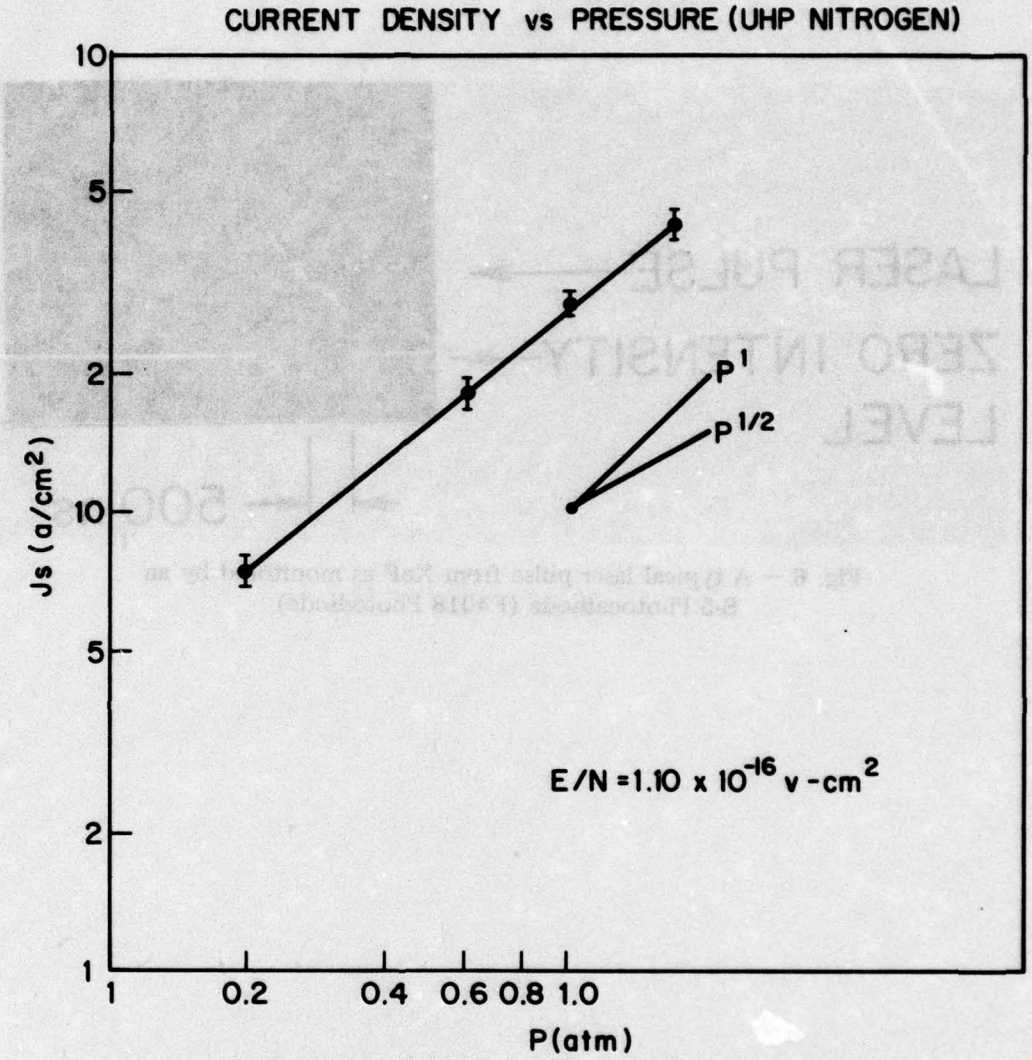

Fig. 5 — Observed sustainer current in ultra-high purity nitrogen for an $E/N = 1.1 \times 10^{-16}$ V-cm^2. Slopes corresponding to P^1 and $P^{1/2}$ pressure dependences are shown.

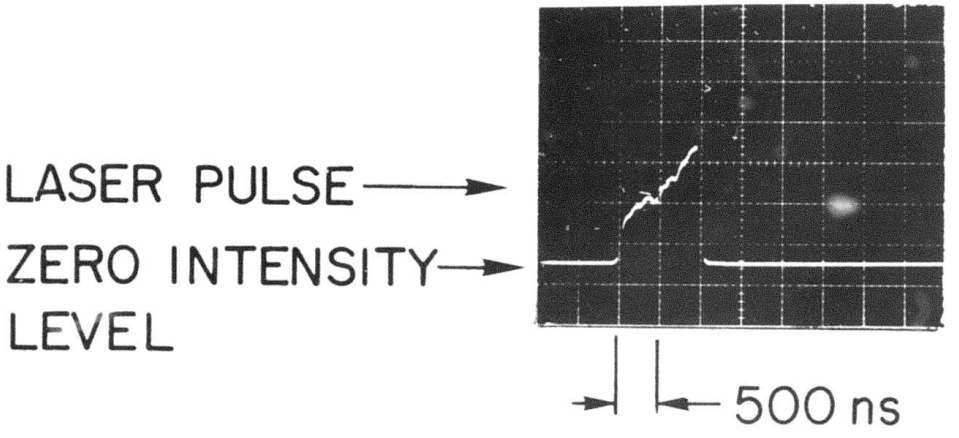

Fig. 6 — A typical laser pulse from XeF as monitored by an S-5 Photocathode (F4018 Photodiode)

References

1. DARPA-NRL Laser Program Semiannual Technical Report, 1 July 1975 to 31 December 1975, NRL Memorandum Report #3341, p. 20 et. seq.

2. Registered trademark of the International Nickel Company, Inc.

3. Registered trademark of the Dupont Co.

4. D. H. Douglas-Hamilton, J. Chem. Phys. 58, 4820 (1973).

5. L. F. Champagne, J. G. Eden, S. K. Searles and N. W. Harris, (to be published).

2. Polyatomic Energy Transfer

The polyatomic energy transfer project was concerned with a) the determination of the energy absorbed by SF_6 from nanosecond duration CO_2 laser pulses, and b) infrared double resonance measurements in SF_6, during this reporting period.

Measurements of pulse energies absorbed by SF_6 were performed for two main reasons. First, while no evidence of self-induced transparency had ever been noted in the double resonance experiments, it was desirable to demonstrate its absence directly so as to ensure that this effect did not complicate the interpretation of the results. Second, because it had been reported by several workers using 200 ns pulses that SF_6 shows no tendency to saturate as the pulse energy and intensity increase, it was important to establish if this would hold true for 2 ns pulses.

Accordingly, energy measurements were made of pulses transmitted by a sample cell containing SF_6 at various pressures between 0.1 and 2.5 torr SF_6. The input pulse energy was monitored by dividing the laser pulse with a beam splitter and detecting the split-off pulse energy with a second energy meter and allowing for the measured reflectivity of the beam splitter. Incident energies were 3-5 mJ for pulses of duration 2 ns (FWHM).

The results are summarized in Table II. Three separate pulses were used at each pressure. No attempt was made to vary the incident energy over a wide range in this experiment.

It is clear from Table II that n, the number of photons absorbed per molecule, is a weak function of the pressure, but would appear to increase in proportion to the incident energy for pressures between 0.6 and 2.5 torr. Furthermore, n is greater than unity and would be still greater if the ratio of the SF_6 absorption bandwidth to the laser-power-broadened width were allowed for. This result is consistent with that obtained by other workers using longer pulses and clearly demonstrates that self-induced transparency is not important under these conditions.

The major effort was in double resonance experiments on SF_6. The apparatus used is shown in Fig. 7. The nanosecond laser is one built in this branch at NRL and emits a train of 2 ns pulses (FWHM) from which one is selected

TABLE II

RESULTS OF ABSORPTION MEASUREMENTS IN SF_6

P_{SF_6} (torr)	E_o (mJ)	E (mJ)	n (Ø molecule^{-1})
2.493	4.13	0.297	1.18
	3.84	0.336	1.08
	3.54	0.396	0.966
1.1513	4.43	1.49	1.96
	3.84	0.99	1.90
	3.84	1.19	1.76
0.998	5.6	3.17	1.87
	5.01	2.52	1.91
	3.84	1.78	1.58
0.606	3.98	2.52	1.85
	3.54	2.28	1.59
	3.54	2.27	1.61
0.3936	4.72	3.71	1.97
	3.84	2.97	1.69
	3.54	2.57	1.89
0.1979	3.84	3.26	2.25
	3.39	2.87	2.01
	2.95	2.08	3.37
0.1007	3.84	3.76	0.609
	3.54	3.51	0.23
	3.25	2.97	2.13

E_o is energy incident on sample

E is energy transmitted by sample

n is number of photons absorbed divided by the total number of SF_6 molecules in the laser beam

for sample excitation. Selected pulse energies were 3-5 mJ. Beam diameter is about 6 mm.

The probe laser is a commercial CW CO_2 laser whose power is controlled by a 1/2 wave plate and analyzer stack. It is grating tunable on the laser lines of the (001-100) and (001-020) bands. The sample cell is a 25.4 mm i.d. stainless steel cylinder fitted with Brewster's angle NaCl windows. It is connected to a glass manifold fitted with greaseless Teflon "0" ring stopcocks. Pressure in the manifold/sample cell is measured by a capacitance manometer. The detector is a Ge:Hg photoconductor biased at -220 Vdc. Its measured risetime is < 1 ns while its falltime is 2.0 ns.

The double resonance experiment itself is illustrated in Fig. 8 for the case of SF_6. The nanosecond pulse on the P(20) line of the 10.6 μ band excites the SF_6 sample to the first excited level ($v_3 = 1$) in the ν_3 vibrational mode at 948 cm^{-1}. At the pump intensities used, it is likely that direct excitation to $v_3 = 2$ and 3 is also occurring, but for simplicity this is not indicated in the figure. After the pulse, excitation is transferred to the other vibrational modes of the molecules by various V-V, R, T, processes. One purpose of the experiment is to measure the rate of these processes. Among the many, closely spaced vibrational levels of the SF_6 molecule an equilibrium is rapidly established permitting a vibrational temperature to be assigned which

is higher than the translational temperature. For clarity, only the six lowest levels are explicitly indicated in Fig. 8. Absorption of the probe laser radiation by these excited levels produces the double resonance signal which is detected. Probe laser absorption by the levels directly pumped must also be considered. This process is illustrated by the large arrow in the upper left hand portion of Fig. 8 and will be discussed below. Ultimately, the system decays back to thermal equilibrium by a combination of V→R, T processes via the lowest vibrational level of the ν_6 mode. This occurs on a time scale of hundreds of microseconds and has already been extensively studied, so very little attention has been given to it here.

The major results of double resonance as a function of probe-laser line are shown in Fig. 9. At the upper left is shown the transient increased absorption observed on every probe line from P(24) to P(36). The rise of this signal was nonexponential and did not vary with SF_6 pressure over the range studied, viz., from 0.5 to 0.1 torr. Added Ar up to 125 torr also made no difference. Consequently, the rising portion of the double resonance signal is interpreted as an integral of the pumping pulse itself, indicating that the V-V rate is so fast that it cannot be resolved even with a 2 ns pulse.

Because the signal rises throughout the nanosecond pulse, rather than becoming saturated at some early time,

the lower pumped levels must be rapidly replenished. Direct evidence of this replenishment is shown in the lower left hand portion of Fig. 9. Here probing with P(20), the line also used for pumping, monitors the levels coupled by the intense laser field. A transient bleaching is observed whose decay time is plotted in Fig. 10 along with the detector falltime. The two values are not well separated, but the equilibrium rate of the pumped transition is estimated to be 2.9 ns for a mixture of 100 mtorr SF_6 and 11.3 torr He. This gives an indication of why SF_6 is so difficult to saturate.

Using probe lines at shorter wavelengths than the pumping line, traces are obtained such as those on the upper and lower right of Fig. 9. At these wavelenghts, the ground state is being probed. Consequently, on the P(10)-P(14) and P(18) lines, a transient increase in transmission is observed to occur on a 100 ns time scale, corresponding to depletion of the ground state levels by pumping. A unique case occurs for the P(12) CO_2 laser line where an additional effect is observed. Here a very rapid rise and fall of transmission precede the slow rise found on the P(18), P(14), and P(10) lines. This indicates that there are SF_6 transitions near 944.2 and 951.2 cm^{-1} which have a level in common. Moreover, the sign of the rapid transmission change is pulse power dependent, indicating that

a coherent transient effect may be taking place. This is not well understood at present, but will be pursued in the future.

One other experiment was to record the double resonance signals as a function of pulse power/energy for the given 2 ns pulse width. This was done to establish whether a lengthening of the double resonance risetime would occur. If so, it would be strong evidence that the radiation field itself was responsible for the rapid energy transfer by coupling the various vibrational modes. The required control was achieved in the same way that the probe laser power is controlled, viz., by means of a 1/2 wave retardation plate and analyzer stack positioned at the output of the pulsed laser. By this means the pulse energy delivered to the sample could be reduced by two orders of magnitude.

The results of this experiment were inconclusive, as the double resonance risetime did not change although the signal amplitude was of course reduced. A further reduction in pulse energy would require double-resonance detection sensitivity beyond that of the present apparatus, so no further power reduction was attempted. Planned installation of a signal averaging system should extend the system's capability sufficiently to warrant further investigations.

Finally, it must be shown that the double resonance signals observed do not result from absorption by the levels

directly pumped by the nanosecond pulse. For this there are four main pieces of evidence. First, comparison of the double resonance absorption coefficient illustrated in Fig. 11 with that of shock heated SF_6 gives roughly the same vibrational temperature at all probe wavelengths. Second, if the absorbed energy is divided by the vibrational and rotational heat capacity, a vibrational temperature increase is obtained which is close to that determined by the first method. These two points together are strong evidence that a vibrational temperature higher than ambient air is established on a nanosecond time scale, rather than all of the excitation remaining in a single vibrational mode.

The third point is that the excited state absorption coefficient determined from these experiments is red shifted by 8 cm^{-1}, as shown in Fig. 11. If this shift were due to the ν_3 mode alone, the best estimated anharmonicity constant would require $v_3 = 5$ for the lower probed level. Under the pumping conditions employed, this is considered unlikely.

The last point involves the existence of two relaxation times to thermal equilibrium. The shorter of these corresponds to the specific V→T step by which the vibrational temperature relaxes back to the translational temperature. The energy released in this step heats the gas translationally and gives rise to the second relaxation time, which corresponds to bulk heat conduction to the walls of the cell.

If the energy deposited in the SF_6 sample remained in the ν_3 mode above, then the amplitude of the slow relaxation should be much smaller than that of the fast relaxation because thermal heating is non specific, and only a small fraction of the energy released in the V-T step will find its way back into the ν_3 mode. Instead of this, it is found that the two relaxation signal intensities are in the following ratio:

$$\frac{I_{BULK}}{I_{V\rightarrow T}} = \frac{C_{VIB}}{C_{TOTAL}}$$

where the C's are heat capacities. This indicates again that the probe laser senses a great number of levels, rather than just the $v_3 = 1$ or 2 levels, and is thus detecting the energy transfer rate of interest.

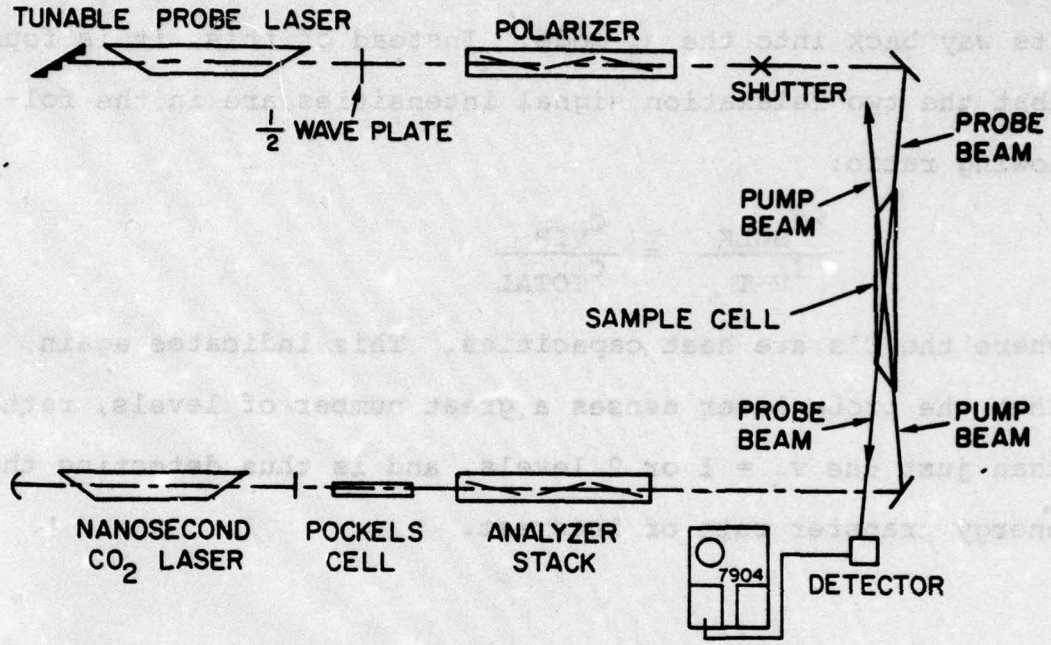

Fig. 7 — Infrared double resonance apparatus. Not shown are a ZnSe lens pair that focuses the probe beam onto the detector and a beam splitter and He-Ne laser which facilitates directing the laser pulse through the sample.

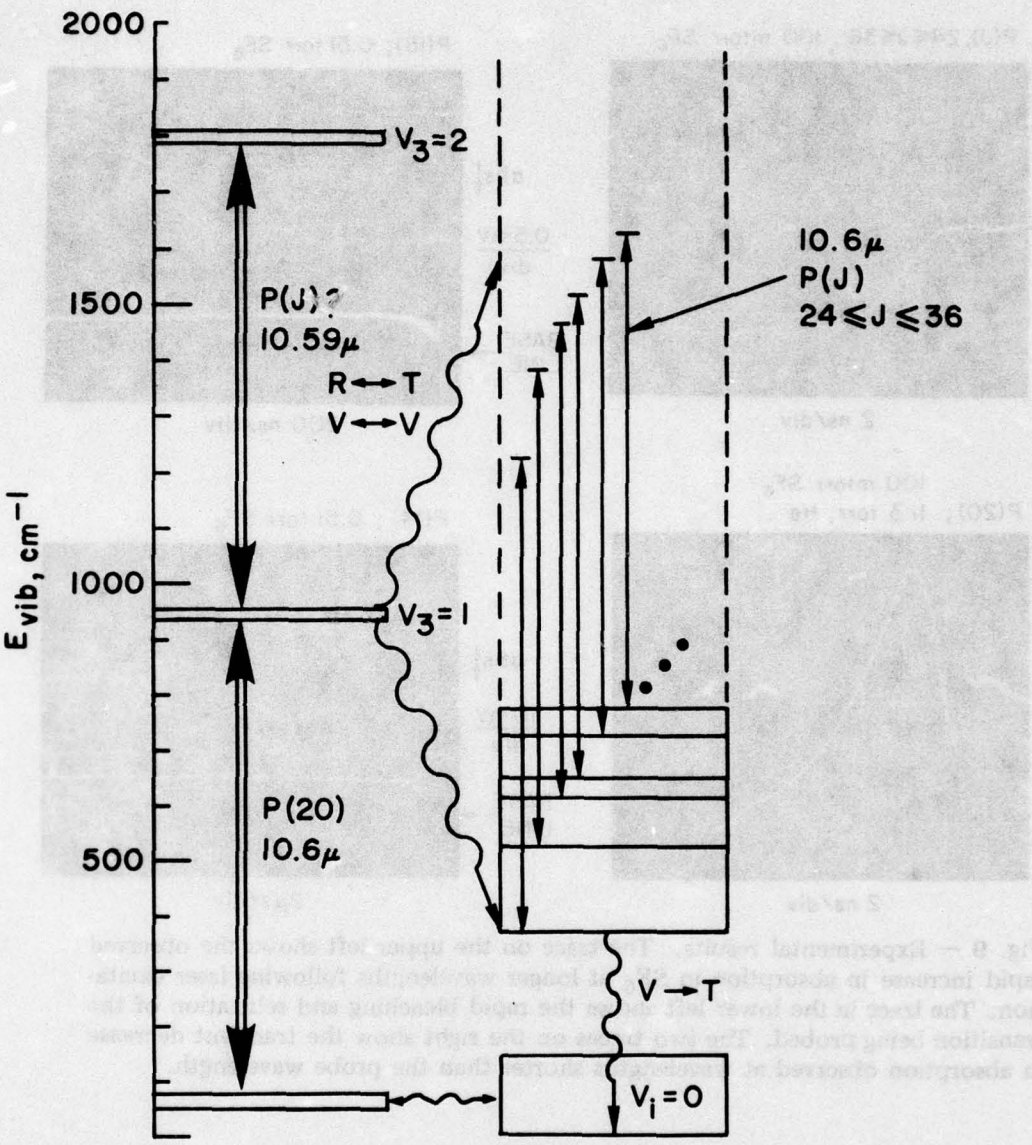

Fig. 8 — Partial energy level scheme for SF_6. The arrows on the left represent pumping of the ν_3 mode by the CO_2 laser pulse to an unspecified upper level. The arrows on the right indicate some of the excited levels being probed. The question of whether the v=2←v=1 transition is being probed is addressed in the text.

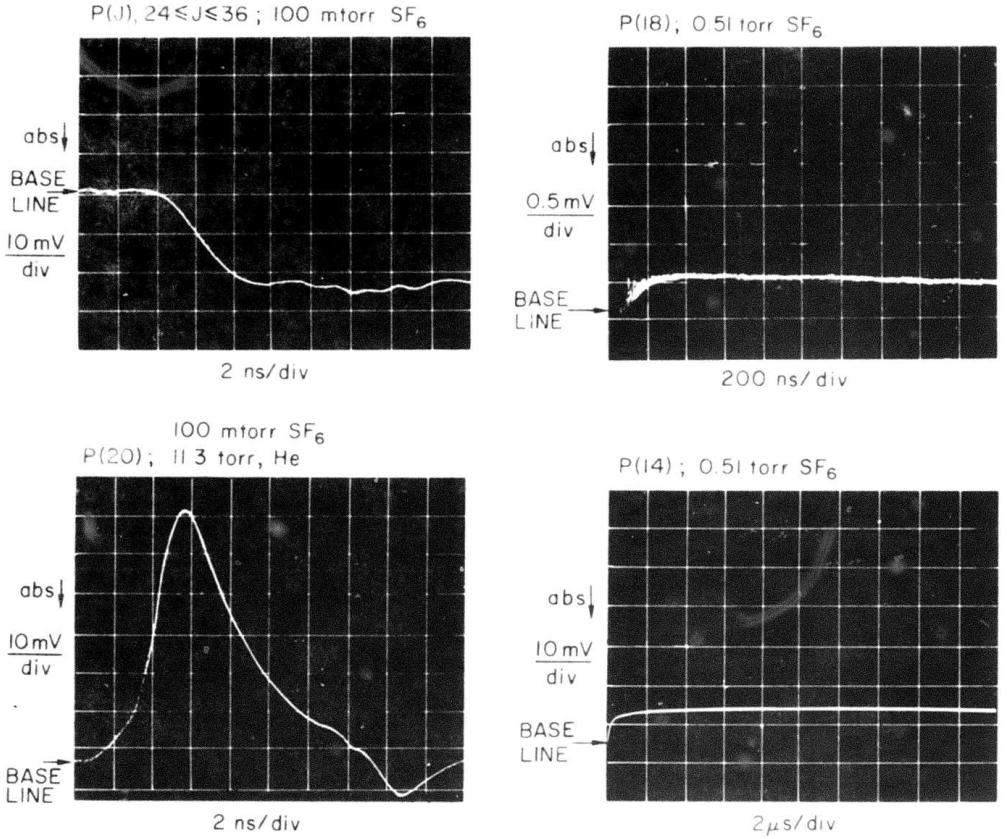

Fig. 9 — Experimental results. The trace on the upper left shows the observed rapid increase in absorption in SF_6 at longer wavelengths following laser excitation. The trace in the lower left shows the rapid bleaching and relaxation of the transition being probed. The two traces on the right show the transient decrease in absorption observed at wavelengths shorter than the probe wavelength.

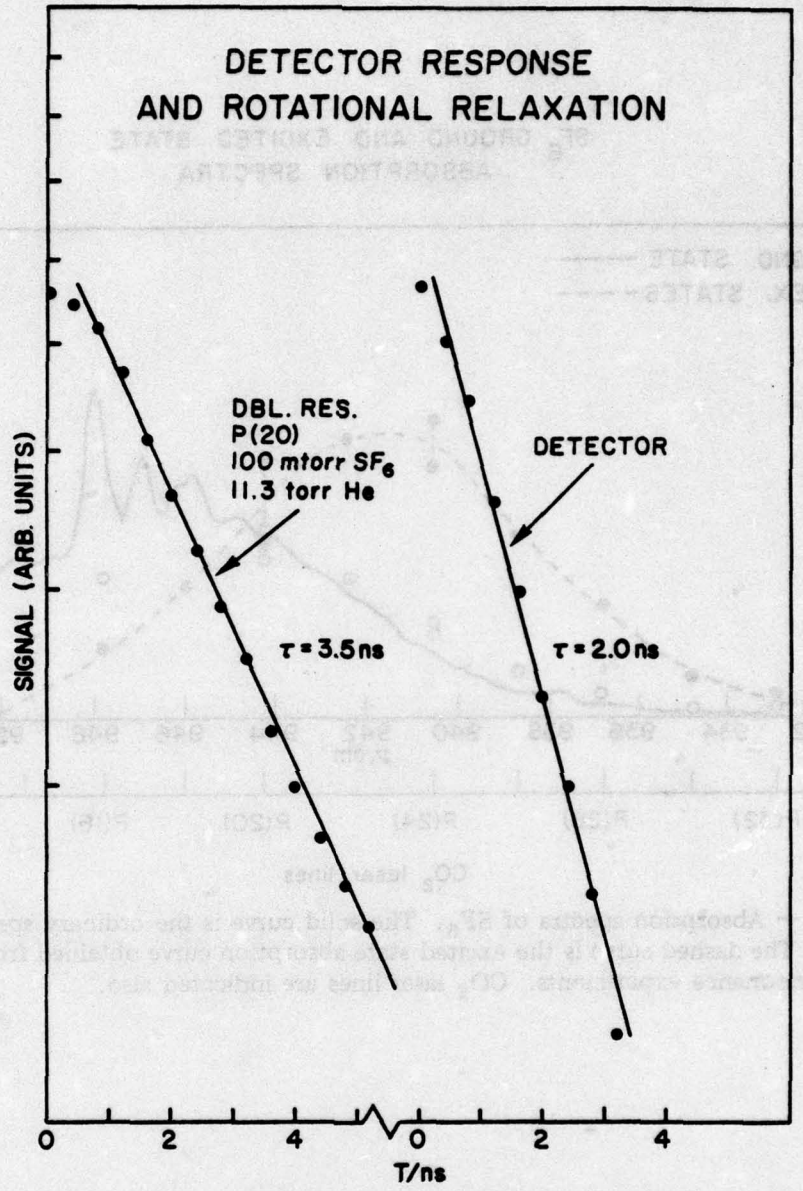

Fig. 10 — Semilogarithmic plots of detector response and double resonance signal. The right band line shows the falltime of the detector's response to a small fraction of a laser pulse. The left band line is the falling part of the curve shown at the lower left of Fig. 9.

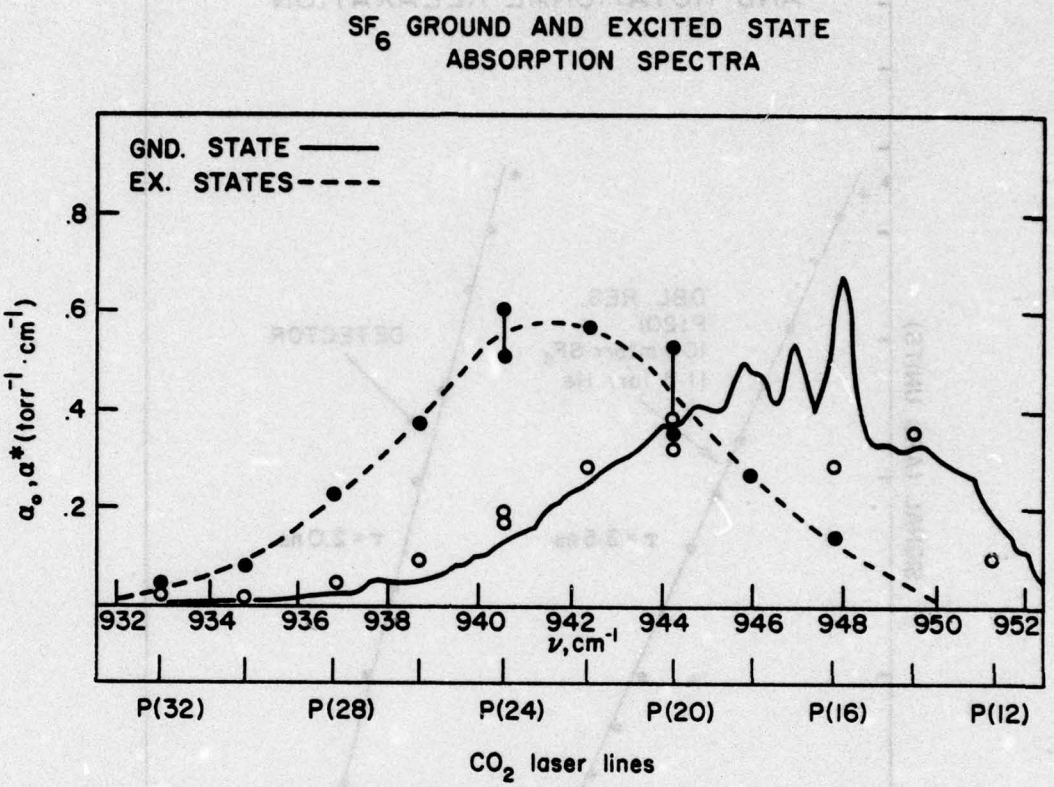

Fig. 11 — Absorption spectra of SF_6. The solid curve is the ordinary spectrum of SF_6. The dashed curve is the excited state absorption curve obtained from the double resonance experiments. CO_2 laser lines are indicated also.

ELECTRICAL INFRARED LASERS

1. Electric Discharge Gasdynamic Lasers

The Electric Discharge Gasdynamic Laser (EDGDL) combines the efficient vibrational excitation of diatomic gases by electron impact with rapid mixing and gasdynamic cooling in a supersonic flow in order to investigate new or more efficient infrared lasers which are populated by energy transfer processes. The NRL facility and results obtained prior to this period have been described in previous reports.[1-4] During this period experiments have resulted in improvements in the power output of the CO-C_2H_2 and CO-CS_2 lasers. The feasibility of a CW HCN laser operating at 3.8 μ has been investigated, and more data pertaining to the proposed D_2-HCl laser have been obtained.

In the initial experiments on the CO-C_2H_2 laser at 8 μ the only output mirror available was a hole coupler with 0.1% transmission and the maximum output observed was 100 mw. Significant improvement in output power has been realized by using a dielectric-coated output mirror with transmission approximately 4%, and by a limited variation of the laser parameters. As shown in Fig. 12, the laser output was found to scale linearly with discharge current up to the 750 ma

limit of the power supplies used. It was found necessary to add a very small amount of oxygen (0.3 torr, approximately 5 millimoles/sec in a 2.5 mole/sec total flow) to the plenum flow in order to achieve good discharge conditions. This technique is well known for CO laser discharges and the mechanism has been discussed in the literature.[5,6] The dependence of laser output on C_2H_2 mass flow is shown in Fig. 13. Higher C_2H_2 mass flows are prevented by the onset of "choking" or spoiling of the supersonic conditions by the injected flow. This leads to heating of the gas and loss of the population inversion, as has been discussed previously.[4] In the initial experiments, it was suspected that acetone present in the acetylene tank might be absorbing at 8 μ thus reducing the laser output. Several experiments have been performed in which the acetylene was cooled prior to injection into the plenum in order to freeze out the acetone. However, no increase in laser power levels was observed when the acetylene was cooled.

During the course of each day's experiments a degradation in laser output was observed. Replacing the windows was necessary to restore the output to a level comparable to that observed at the beginning of the day. Spectrophotometer traces revealed an increase in window transmission of approximately 1% after use. It is hypothesized that an absorbing film is deposited on the windows during operation

of the EDGDL, although the source of this deposit has not yet been determined. Radiant heating of the windows seems to retard the degradation of the laser output. Since such a small loss has a great effect on laser output the gain is obviously low. However, significant energy is stored in the gas and should be extractable using a multi-pass cavity. For discharge conditions for which 15 watts was observed from C_2H_2, 18 watts was extracted from CO, using a similarly transmissive mirror. These data indicate the high efficiency of energy transfer from CO to C_2H_2.

In addition to variations in laser conditions due to window transmission, impurities in the CO used may be responsible for day to day differences observed in laser output. The CO used to date has been commercial grade 98% purity, and impurities could affect the discharge and lead to less efficient excitation of the CO.[7] Higher purity CO has been ordered to test this possibility.

Experiments with the CO-CS_2 laser have resulted in an improvement in power output of a factor of two over that previously reported. In contrast to the C_2H_2 laser, the output from CS_2 does not scale with discharge current into the CO, severely limiting the laser as shown in Fig. 14. As in the case of C_2H_2, "choking" limits the CS_2 mass flow to the value shown in Fig. 15. Modification of the supersonic cavity is expected to alleviate the choking effect,

allowing higher mass flows of injected species and therefore higher power densities.

A number of reasons may be advanced to explain the current dependence of the CS_2 laser.

1. The pumping may be dependent on CO level populations which do not scale with current.

2. The inversion may be saturated because of a lower level bottleneck.

3. Current-dependent dissociation of CS_2 may occur.

The last possibility, CS_2 dissociation, might be due to the dependence of helium metastable population or oxygen atom density on current. Oxygen must be added to maintain the discharge above 300 ma, but it is seen to have no effect on the CS_2 laser below 300 ma. Also, the oxygen concentration is too small to strongly affect the laser output. Dissociation of CS_2 as indicated by visible emission occurs in the absence of CO but this emission disappears as the CO is turned on. At the E/N of the discharge in the He-CO-O_2 mixture, less than 15% of the energy is expected to go into electronic excitation. While dissociation due to He* cannot be ruled out, the other possible reasons for the observed current dependence are more plausible and require examination since they operate through the laser pumping mechanism.

Analysis of the CS_2 laser is complicated by the fact that a number of laser pumping and inversion schemes are

possible, in contrast to the case of the CO-C_2H_2 laser. The C_2H_2 laser operates from the $0100^{o}0^{o}$ to the $0000^{o}1$ levels with the upper state, at 1974 cm^{-1}, being in close resonance with the v=8 → 7 and v=7 → 6 CO transitions at 1955 cm^{-1} and 1982 cm^{-1}. The populations of the v=8 and 7 levels will increase with current, and furthermore are apparently enhanced by the addition of oxygen to the discharge.[5] The behavior of the C_2H_2 laser supports this hypothesis.

Possible CO-CS_2 schemes are shown in Fig. 16. The most probable channels are:

I
- A $CO(v=1) + CS_2(000) \rightarrow CO(v=0) + CS_2(101) + \Delta E = -41\ cm^{-1}$
- B $CS_2(101) + CS_2(000) \rightarrow CS_2(100) + CS_2(001) + \Delta E = 8\ cm^{-1}$
- C $CS_2(100) + He \rightarrow CS_2(000) + He + \Delta E = 658\ cm^{-1}$
- D $CS_2(001) \rightarrow CS_2(100) + h\nu$

or

- E $CS_2(101) \rightarrow CS_2(200) + h\nu$

II
- A $CO(v=9) + CS_2(000) \rightarrow CO(v=8) + CS_2(01^{1}1) + \Delta E = -4\ cm^{-1}$
- B $CS_2(01^{1}1) + CS_2(000) \rightarrow CS_2(001) + CS_2(01^{1}0)$
- C $CS_2(001) \rightarrow CS_2(100) + h\nu$

or

- D $CS_2(01^{1}1) \rightarrow CS_2(11^{1}0) + h\nu$

and

III $\begin{cases} \text{A} & CO(v=24) + CS_2(000) \rightarrow CO(v=23) + CS_2(001) + \Delta E = -9\ cm^{-1} \\ \text{B} & CS_2(001) \rightarrow CS_2(100) + h\nu \end{cases}$

Although the rate for direct pumping of $CS_2(001)$, reaction III-A, is probably much larger than that for the multiquantum pumping processes (I and II), the population of v=24 should be insufficient to make Channel III important. Channel I is favored over Channel II for a number of reasons. The v=1 population is expected to be much greater than $v \geq 7$. The transfer rate for I-A has been measured to be large,[8] and both optically pumped and e-beam pumped CS_2 lasers operate through Channel I.[9,10] Reaction I-E does not seem to be an important process since the cessation of laser oscillation in the EDGDL, when choking raises the translational temperature, indicates that the lower laser level is near the ground state. Furthermore, I-B is very fast, so that I-D must be the dominant laser transition. An inversion by this scheme depends on quenching of the lower laser level population, equally produced with the upper level (I-B), by helium (I-C). Therefore, the rollover in current may be due, in part, to bottlenecking of the inversion by the accumulation of species in the (100) level as a result of insufficient quenching by the helium. Since Channel I is pumped by the v=1 level of CO, differences in the current dependence of the v=1 and $v \geq 7$ could account for the difference in CS_2 and C_2H_2 current dependence. Calculations for low pressure discharges indicate

that the excitation rate[11] and net power[12] into the v=1 level decreases while those of $v \geq 7$ increase as the current and vibrational temperature increase. By altering the discharge, impurities in the CO may contribute to this effect.

Channel II operating in conjunction with Channel I,[13] has been postulated for a high-pressure CS_2 laser and should take place in the EDGDL where significant populations of the $v \geq 7$ levels exist. Further research should indicate definitely the laser channels and current dependence mechanism.

On the basis of observation of fluorescence from HCN after energy transfer from vibrationally excited N_2, D_2, and H_2,[14] attempts were made to demonstrate a laser using this system. These were unsuccessful. Fluorescence measurements indicated that the transfer was not sufficiently fast enough for lasing, and subsequent to the experiments it was learned that deactivation of the proposed upper laser level had been measured to be extremely rapid.[15] In the course of the experiments, however, CO_2 lasing after transfer from excited H_2 was observed. While this is the first observation of lasing from this system, it is noted that the output is weak.[16]

References

1. DARPA-NRL Laser Program Semiannual Technical Report, 1 January - 30 June 1974, NRL Memorandum Report 3005.

2. DARPA-NRL Laser Program Semiannual Technical Report,

1 July - 31 December 1974, NRL Memorandum Report 3084.

3. DARPA-NRL Laser Program Semiannual Technical Report, 1 January - 30 June 1975, NRL Memorandum Report 3217.

4. DARPA-NRL Laser Program Semiannual Technical Report, 1 July - 31 December 1975, NRL Memorandum Report 3341.

5. H. Keren, P. Avivi and F. Dothan, IEEE J. Quantum Elect. QE-11, 590 (1975).

6. H. Keren, P. Avivi, and F. Dothan, IEEE J. Quant. Elect. QE-12, 58 (1976).

7. J. W. Rich and R. C. Bergman, U. S. Air Force Avionics Laboratory Technical Report AFAL-TR-75-5, February 1975.

8. J. K. Hancock, D. F. Starr and W. H. Green, J. Chem. Phys. 61, 3017, 1974.

9. H. Kildal and T. F. Deutsch, Appl. Phys. Lett. 27, 500 (1975).

10. F. O'Neill and W. T. Whitney, Appl. Phys. Lett. 28, 539 (1976).

11. F. T. Wu, W. M. Yu and E. A. Lundstrom, Appl. Phys. Lett. 25, 463 (1974).

12. W. L. Nighan, Appl. Phys. Lett. 20, 96 (1972).

13. L. Y. Nelson, C. H. Fisher and S. R. Byron, Appl. Phys. Lett. 25, 517 (1974).

14. J. M. Fluornoy and L. Y. Nelson, Chem. Phys. Lett. 6, 521 (1970).

15. T. A. Cool, private communication.

16. B. L. Wexler and J. A. Stregack, Optics Comm. 18, 127 (1976).

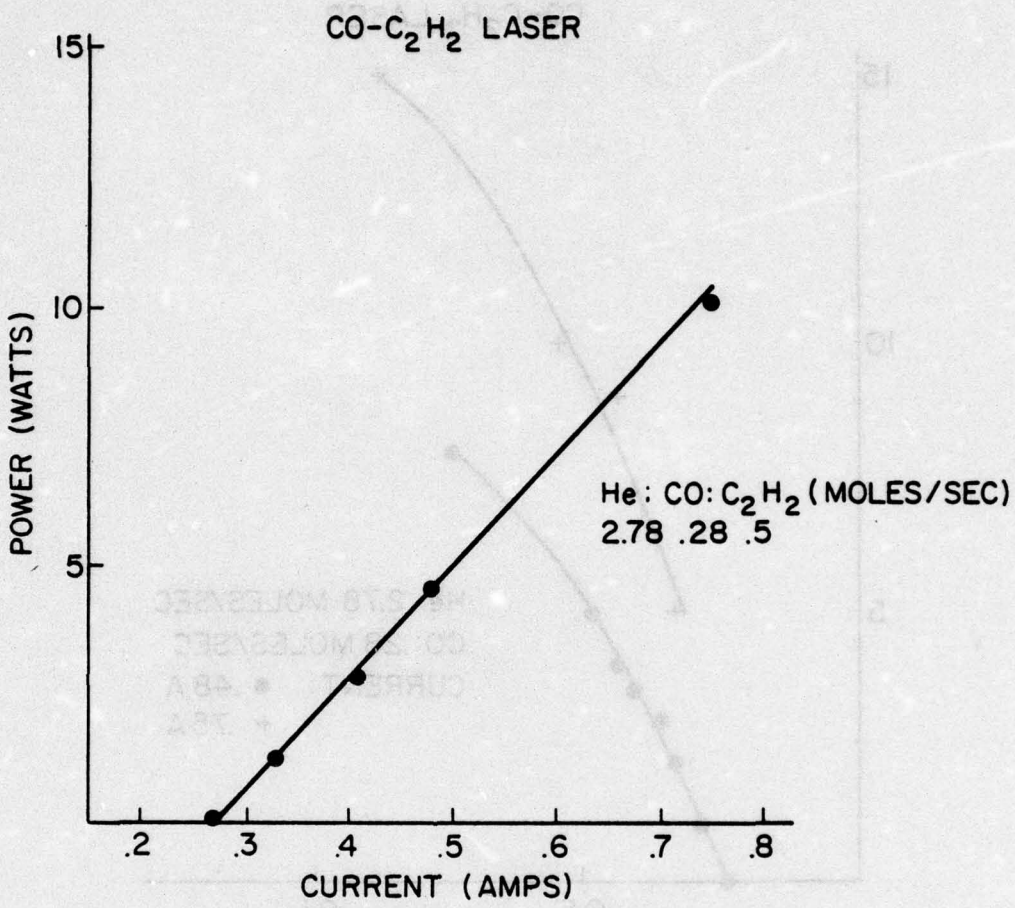

Fig. 12 — C_2H_2 laser output vs. discharge current

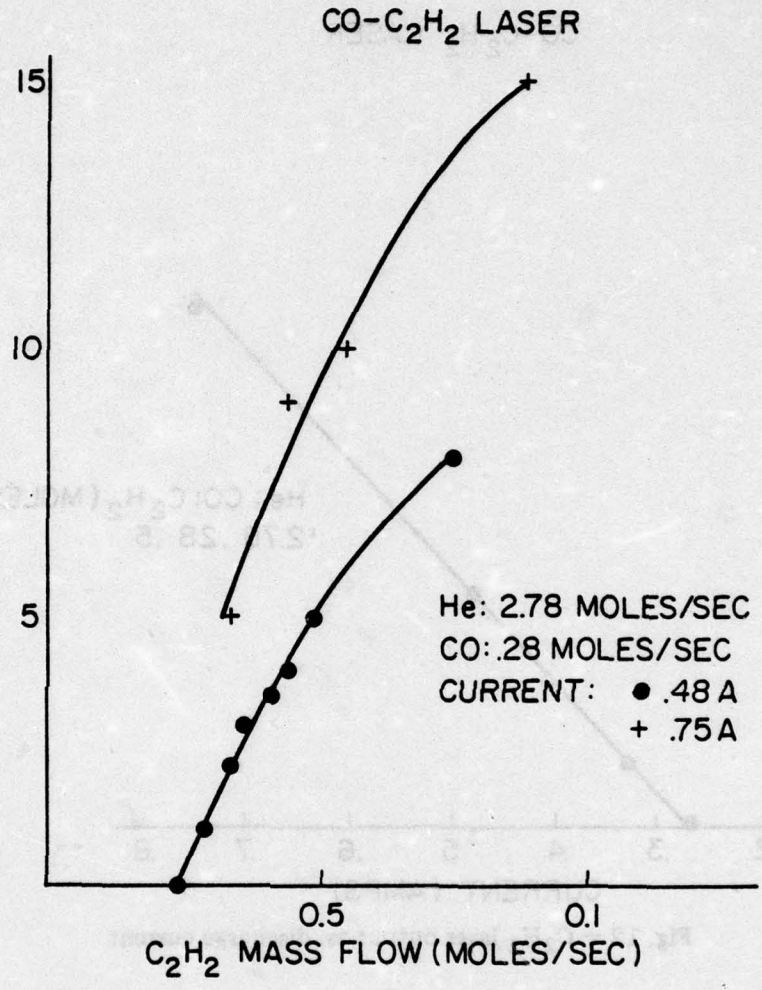

Fig. 13 — C_2H_2 laser output (watts) vs. C_2H_2 mass flow

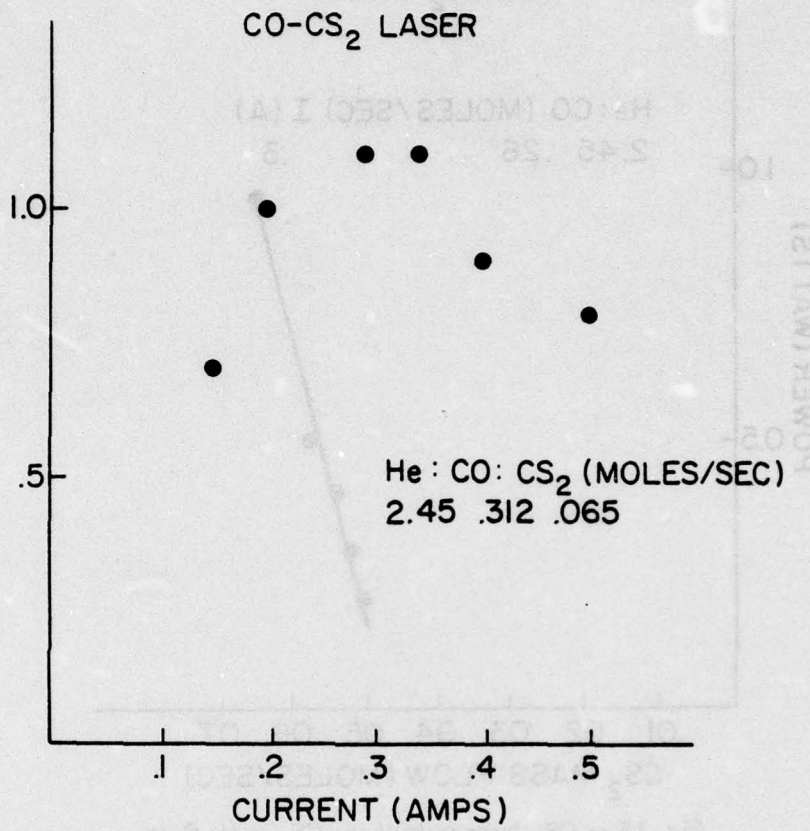

Fig. 14 — CS_2 laser output (watts) vs. discharge current

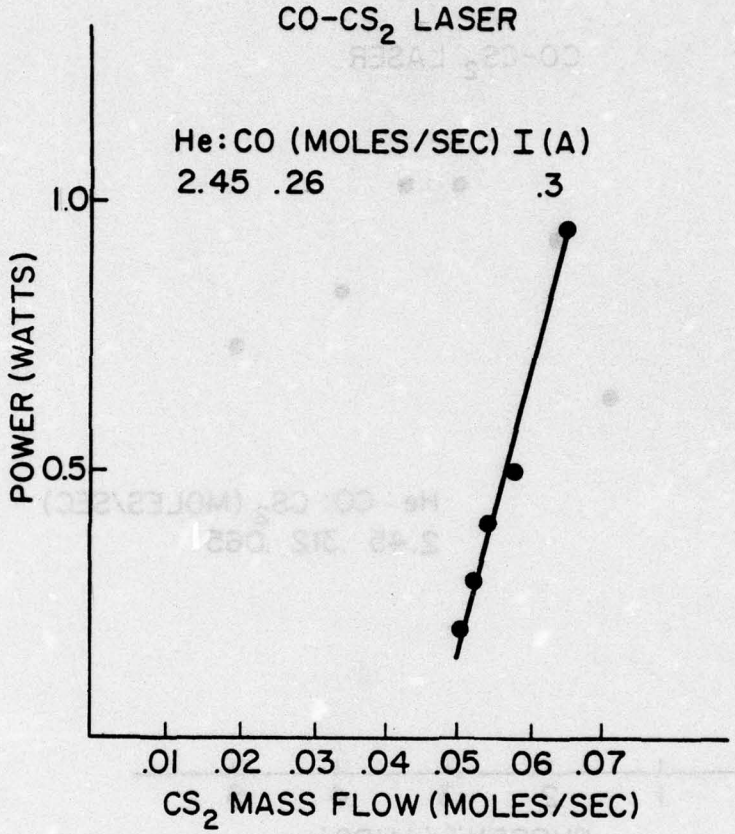

Fig. 15 — CS_2 laser output vs. CS_2 mass flow

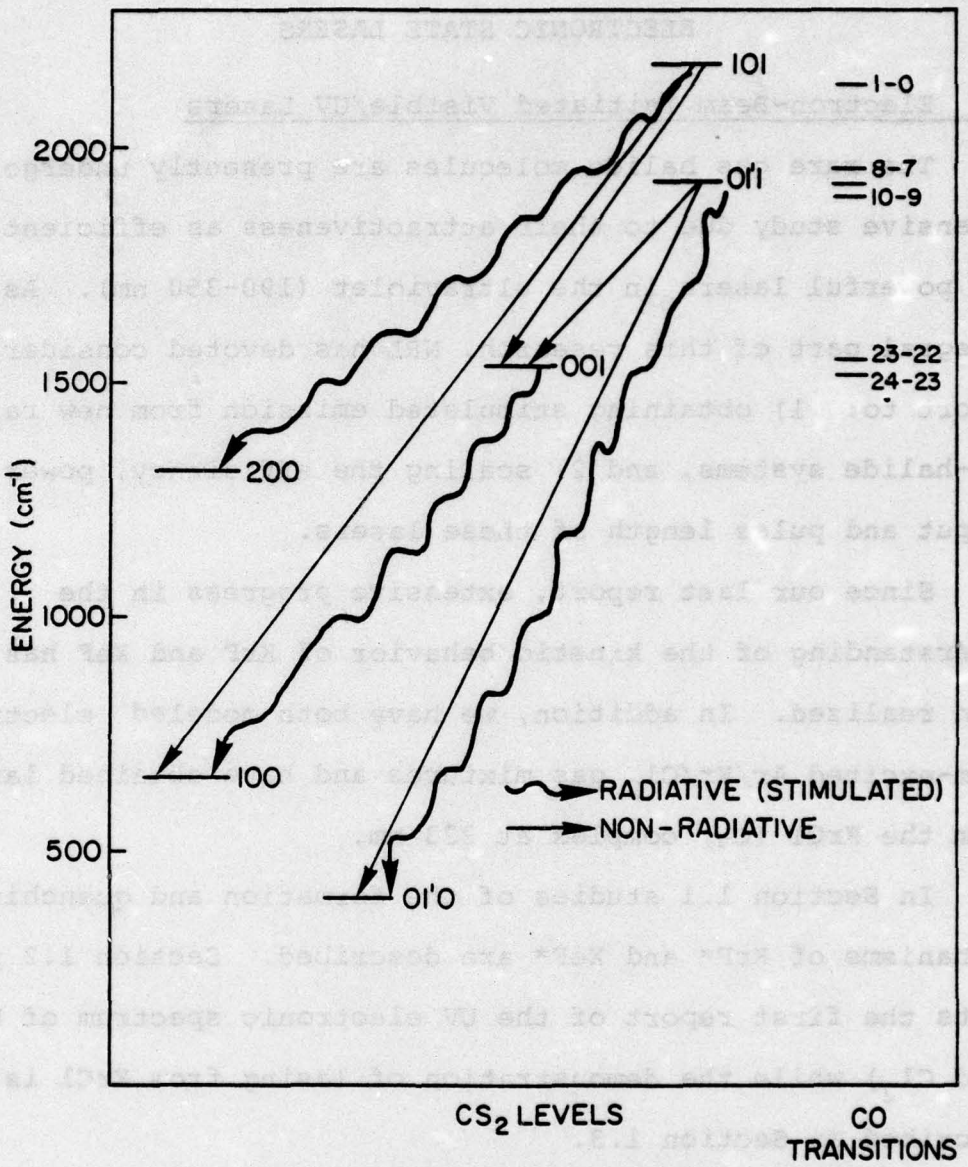

Fig. 16 — Relevant energy levels of the CO-CS_2 transfer laser

ELECTRONIC STATE LASERS

1. Electron-Beam Initiated Visible/UV Lasers

The rare gas halide molecules are presently undergoing intensive study due to their attractiveness as efficient and powerful lasers in the ultraviolet (190-350 nm). As an integral part of this research, NRL has devoted considerable effort to: 1) obtaining stimulated emission from new rare gas-halide systems, and 2) scaling the efficiency, power output and pulse length of these lasers.

Since our last report, extensive progress in the understanding of the kinetic behavior of KrF and XeF has been realized. In addition, we have both modeled electron beam-excited $Ar/Kr/Cl_2$ gas mixtures and have obtained lasing from the KrCl ($C\frac{1}{2}$) complex at 223 nm.

In Section 1.1 studies of the formation and quenching mechanisms of KrF* and XeF* are described. Section 1.2 presents the first report of the UV electronic spectrum of F_2 (and Cl_2) while the demonstration of lasing from KrCl is described in Section 1.3.

1.1 Formation and Quenching of XeF and KrF Excited Electronic States

The mechanism responsible for the formation of the XeBr exciplex[1] has been previously reported.[2,3] The

following processes were utilized to predict the temporal behavior of XeBr* emission following e-beam excitation of low-pressure Xe-Br_2 gas mixtures:

$$e + Xe \rightarrow Xe^* + e \quad (1)$$

$$Xe^* + Br_2 \xrightarrow{k_2} XeBr^* + Br, \quad (2)$$

$$XeBr^* \xrightarrow{k_3} Xe + Br + h\nu\ (2818\ \text{Å}) \quad (3)$$

By comparing the predicted fluorescence profiles with those obtained experimentally, the exciplex formation and radiative decay constants, k_2 and k_3, were determined.

An extension of this approach to the KrF and XeF systems was sought. The efficient and powerful lasing in the ultraviolet which has been reported for these rare-gas monohalides[4-6] has created great interest in the physical processes by which the excited rare-gas halide states are formed and destroyed in electron-beam (e-beam)-produced plasmas. The studies to be described here clearly show that a three-step model (such as Eqs. (1)-(3)) is inadequate for the XeF and KrF molecules.

In these experiments, Xe (or Kr)/He/1% F_2 gas mixtures were irradiated with a 433-kV 50-ns FWHM electron beam (the e-beam device has been described in detail elsewhere).[2] The resulting side-fluorescence was monitored by an ITT F4018 (S-5) photodiode. Utilizing a 0.75-m Jarrell-Ash monochromator and EMI 9816 (S-20) photomultiplier combination, the XeF and KrF emission bands were viewed with 3-Å resolution.

Time-integrated spectra were obtained by exposing Polaroid type 55 (for XeF) or Kodak 101-01 VUV (for KrF) film to the fluorescence. The rare gases used in these experiments were 99.995% pure, the stated purity of the fluorine was 98%. Gas mixtures in the stainless steel cell were replaced after each shot.

Reactions (1)-(3) may be rewritten for the XeF* complex:

$$e + Xe \rightarrow Xe^* + e \quad (4)$$

$$Xe^* + F_2 \xrightarrow{k_5} XeF^* + F \quad (5)$$

$$XeF^* \xrightarrow{k_6} Xe + F + h\nu\ (3511\ \text{Å}) \quad (6)$$

A similar set of relations hold for KrF*.

To determine if (4)-(6) comprise an adequate representation of the KrF and XeF exciplex formation and decay kinetics, measurements of the XeF* (3511 Å) and KrF* (2480 Å) time-resolved emission waveforms for various gas mixtures were conducted. Specifically, the role of Xe and Kr in quenching XeF* and KrF*, respectively, was examined. Equations (4)-(6) do not account for the nonradiative process:

$$RF^* + R \xrightarrow{k_7} 2R + F,\ (R = Xe, Kr) \quad (7)$$

and therefore predict no variation in the RF* emission waveform FWHM as the diluent (rare gas) pressure is increased.[7] However, the XeF* fluorescence FWHM was observed to decrease by 9% and KrF* by 30% (see Fig. 17) as the rare-gas pressure (Xe and Kr, respectively) was increased from 25 to 50 Torr. (Further temporal narrowing of the optical pulse at higher

pressures, > 100 Torr, is not of great interest since, in this regime, three-body collisional processes must be considered.) Therefore, Fig. 17 suggests that Eqs. (4)-(6) are inadequate as a description of XeF and KrF exciplex kinetic processes at low pressures.

Further studies were undertaken to determine the possible participation of helium in process (7). The helium was originally introduced into these experiments since F_2 was available to us only in He/2% F_2 mixtures. This was not expected to complicate the exciplex formation kinetics due to energy transfer from excited helium states since helium, for all but the highest pressures reported here, is transparent to the electron beam.[8]

However, the addition of helium to Xe (or Kr)-F_2 mixtures significantly decreased the XeF* and KrF* emission FWHM as shown in Fig. 18. Surprisingly, though, increasing helium density also strongly enhanced the rare-gas-fluoride fluorescence amplitude (cf. Fig. 19). Spectral profiles taken of the XeF and KrF bands were found to be helium pressure independent, indicating that this enhancement is not due to vibrational relaxation of the excited molecule.

A possible explanation for the observed spontaneous emission behavior assumes that there exist two rare-gas excited states, R* and R**, and that each reacts with F_2 to form RF* (R = Xe and Kr, as before). If it is further

postulated that the cross section for the formation of RF* in a collision of R** with F_2 is small compared to that for R* and F_2, then helium merely serves to deactivate R** to R*. Quenching of the argon $^3P_2$ metastable state by CO has been shown to proceed an order of magnitude faster than the analogous process for Ar*($^3P_0$).[9] Thus, the mechanisms suggested here are reasonable, although the observations can probably also be explained assuming the existence of two ionic rare-gas-fluoride states. Due to radiation trapping, the Xe and Kr $^3P_1$ and $^1P_1$ resonance states are effectively metastable over the time scale of this experiment (τ < 150 ns). It is conceivable, therefore, that these resonance levels are participating in the formation of RF* molecules. Measurements of the quenching rates of the Xe and Kr metastable ($^3P_2$ and $^3P_0$) states by F_2 would clarify the processes responsible for the data of Figs. 18 and 19.

Electron collisional quenching of the XeF and KrF excited state populations has also been studied. Figure 20 illustrates the effect of varying the electron-beam intensity[10] (i.e., flux) and helium pressure on the fluorescence FWHM of KrF*. (Similar results were obtained for XeF*.) The reduction of the KrF* emission FWHM with increasing e-beam intensity (fixed He) suggests that excited molecules are being destroyed through impact ionization or dissociative attachment:

$$e\ (E < 5\ eV) + KrF^* \xrightarrow{k_8} Kr^+ + F^- + e \quad (8)$$

$$\text{or } KrF^+ + 2e$$

$$e + KrF^* \xrightarrow{k_9} Kr + F^- \quad (9)$$

Huber and co-workers[11] have recently shown impact ionization of Xe_2^* to be a significant process for the Xe_2 laser. Finally, electron cooling through helium collisions does not appear to be an important mechanism (see Fig. 20). Obviously, such cooling of low-energy electrons would tend to inhibit reactions (8) and (9).

Observation of electron quenching of XeF* and KrF* points out the difficulty of performing kinetic studies of these molecules in e-beam-excited plasmas. As a result, it is difficult to estimate the spontaneous lifetimes of the KrF and XeF excited species and the deactivation rates of these molecules by Kr and Xe, respectively. Modeling of these systems was not performed since (i) the rate constants k_7-k_9 are not known,[12] and (ii) a large number of rate constant value combinations would fit the data. Figure 3 of Ref. 3 shows that even for a three-process model the theoretical predictions are not extremely sensitive to variations of the kinetic process rates.

In summary, the objective of this work was to determine two important rate constants (for the XeF and KrF exciplex systems) using a three-step model previously employed for XeBr. The results indicate that a more complex kinetic

scheme is necessary to describe the XeF and KrF emission data. Specifically, collisional quenching of KrF* (and XeF*) by electrons (ionization or attachment) and the rare gases must be incorporated into a realistic representation of these systems. The identification of these additional mechanisms constitutes an important step towards a better understanding of the behavior of electrically excited KrF and XeF lasers.

References

1. Exciplex ("excited complex") is used to refer to an excited heteronuclear diatomic molecule with an unbound ground state. A more precise definition is given in M. Gordon and W. R. Ware, *The Exciplex* (Academic, New York, 1975).

2. S. K. Searles and G. A. Hart, Appl. Phys. Lett. 27, 243 (1975).

3. G. A. Hart and S. K. Searles, J. Appl. Phys. 47, 2033 (1976).

4. J. J. Ewing and C. A. Brau, Appl. Phys. Lett. 27, 350 (1975).

5. G. C. Tisone, A. K. Hays, and J. M. Hoffman, Opt. Commun. 15, 188 (1975).

6. M. L. Bhaumik, R. S. Bradford, Jr., and E. R. Ault, Appl. Phys. Lett. 28, 23 (1976).

7. This can readily be proven analytically for two special cases: (a) steady state and (b) instantaneous production of Xe*, assuming $k_5(F_2) \simeq k_6$. General cases may be demonstrated using numerical integration.

8. M. J. Berger and S. M. Seltzer, NASA Report SP-3012, 1964 (unpublished).

9. L. G. Piper, J. E. Velazco, and D. W. Setser, J. Chem. Phys. 59, 3323 (1973).

10. Changes in the e-beam flux were effected by changing the diode gap or by reducing the storage capacitors' charging voltage.

11. E. E. Huber, Jr., L. R. Jones, E. V. George, and R. M. Lerner, IEEE J. Quantum Electron. QE-12, 353 (1976).

12. Although the e-beam flux can be measured using blue cellophane dosimetry, estimating k_8 and k_9 from the data of Fig. 4 would be difficult.

1.2 Ultraviolet Emission Spectra from $Ar-F_2$ and $Ar-Cl_2$ Mixtures

The halogens have aroused considerable interest recently as laser candidates in the ultraviolet. Stimulated emission on the E→B bands of I_2 and the D→X bands of Br_2 has been observed using either electron beam or discharge excitation.[1-3] Moreover, a potential Cl_2^* dissociation laser was recently proposed by Chen and Payne.[4]

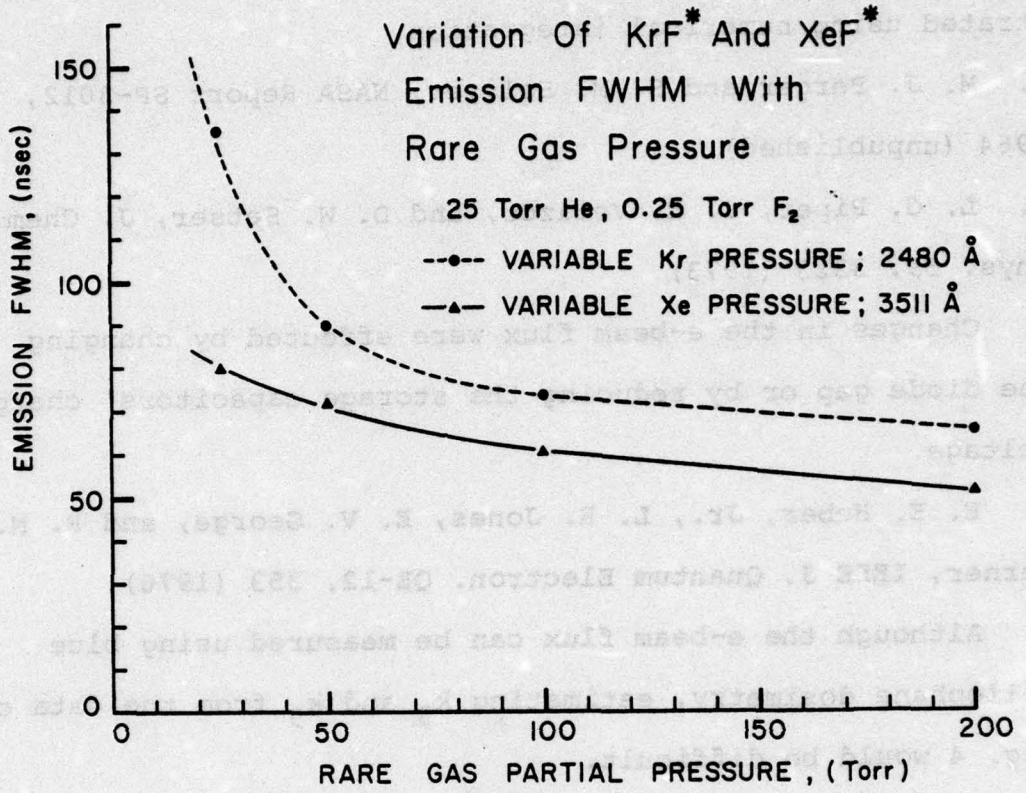

Fig. 17 — Effect of rare-gas pressure on KrF* and XeF* emission FWHM for P_{He} = 25 Torr and P_{F_2} = 0.25 Torr. Top curve: quenching of KrF* by Kr; bottom curve: quenching of KrF* by Xe.

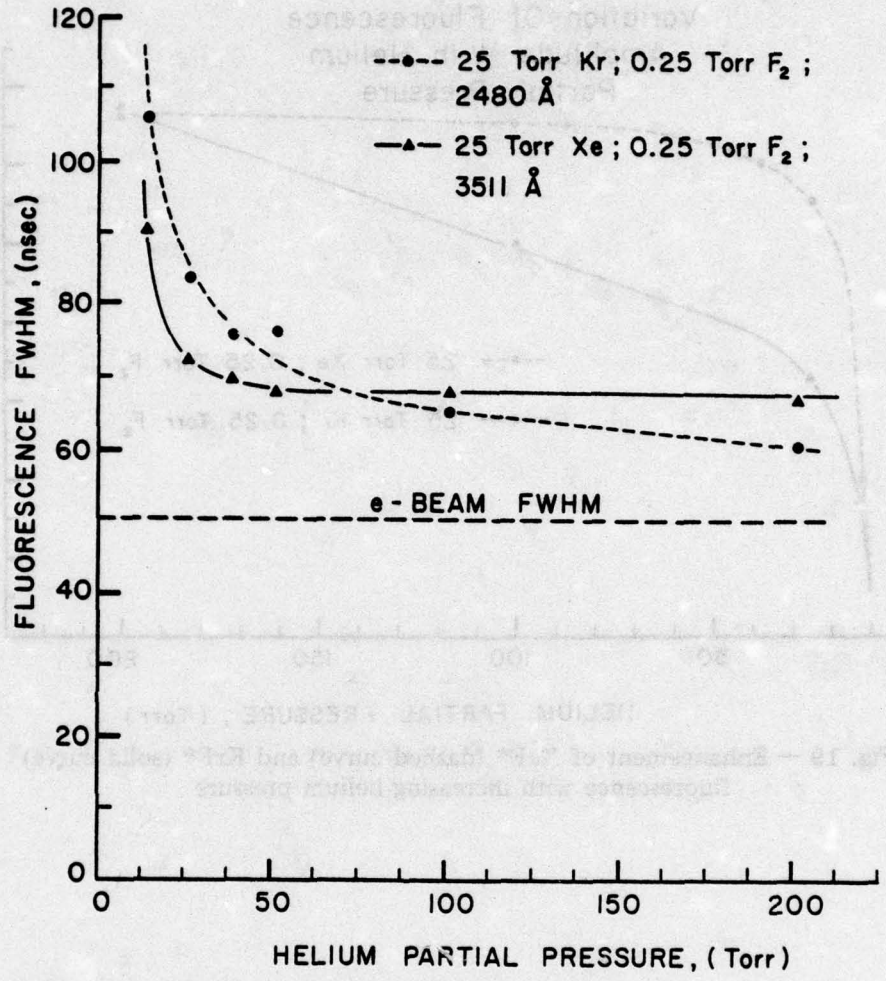

Fig. 18 — Variation of KrF* (dashed curve) and XeF* (solid curve) emission FWHM with increasing helium pressure

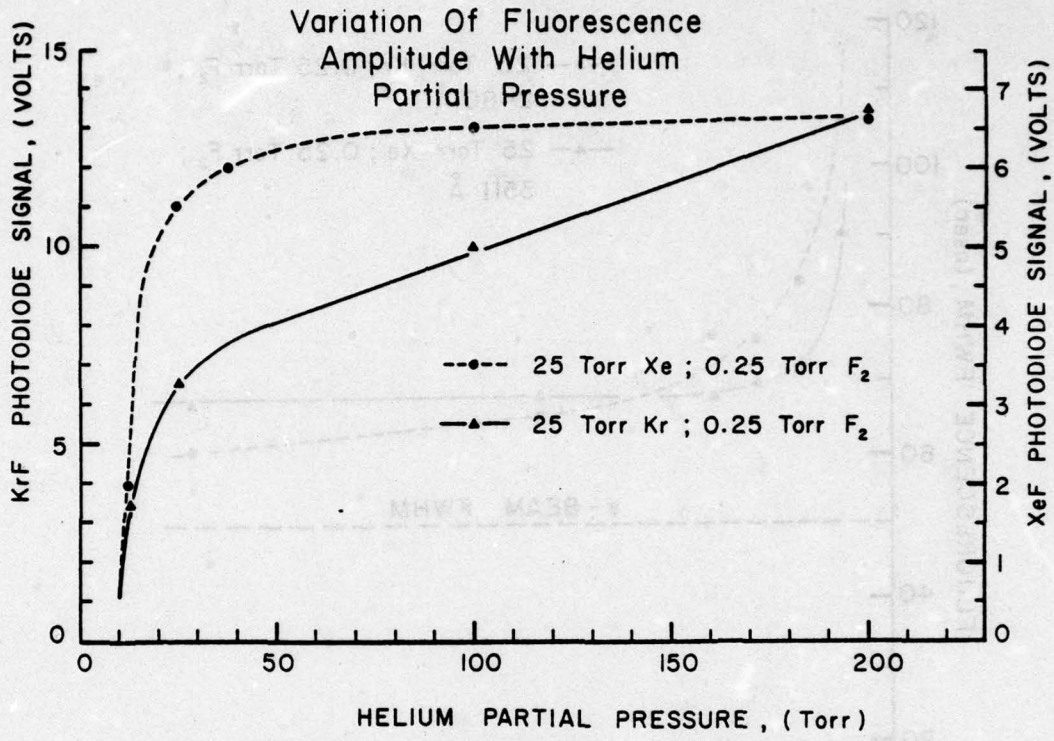

Fig. 19 — Enhancement of XeF* (dashed curve) and KrF* (solid curve) fluorescence with increasing helium pressure

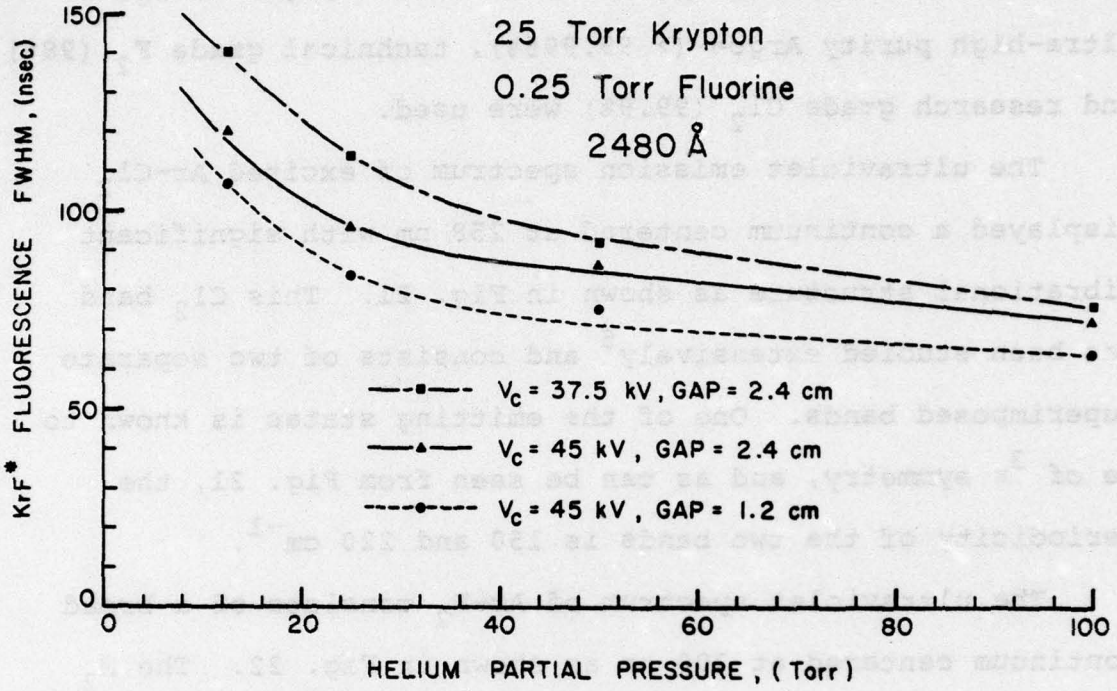

Fig. 20 — Emission FWHM of KrF* as a function of helium pressure and e-beam pumping intensity. The plasma diode was gapped and the charging voltage V_c was reduced such that the integrated KrF* fluorescence intensity had the following relative values (●) 1.0; (▲) 0.1; and (■) 0.05.

In this section the emission spectra of high pressure, electron beam excited Ar/F_2 (Cl_2) gas mixtures are presented and the kinetics briefly discussed. The gas compositions were 1000-3000 torr Ar with 0.5-5.0 torr halogen additive. Ultra-high purity Argon (> 99.995%), technical grade F_2 (98%), and research grade Cl_2 (99.9%) were used.

The ultraviolet emission spectrum of excited $Ar-Cl_2$ displayed a continuum centered at 258 nm with significant vibrational structure as shown in Fig. 21. This Cl_2 band has been studied extensively[5] and consists of two separate superimposed bands. One of the emitting states is known to be of $^3\pi$ symmetry, and as can be seen from Fig. 21, the periodicity of the two bands is 150 and 220 cm^{-1}.

The ultraviolet spectrum of $Ar-F_2$ consists of a broad continuum centered at 300 nm as shown in Fig. 22. The N_2 C→B bands at 337.1 and 357.7 nm and Hg atomic lines were used for wavelength calibration. The relative absorption spectrum of F_2 is also shown in Fig. 22. Note that increasing the F_2 partial pressure by an order of magnitude shifts the peak continuum emission towards shorter wavelengths despite the maximum in the F_2 absorption spectrum at 284 nm.[6-8] Utilizing either F_2 or HF as the fluorine donor yielded identical spectra.

From our experimental observations with both $Ar-Cl_2$ and $Ar-F_2$, we tentatively assigned the 300 nm continuum to

F_2 in accord with theoretical calculations of Hay and Cartwright.[9] However, more recently, other investigators have assigned this continuum to Ar_2F.[10]

Although little is presently known of the formation mechanism of these kinetic complexes, recent experimental results[4] suggest that the continua are formed by direct energy transfer from metastable Ar_2^* (1 μ) molecules. This would explain the strong dependence of the fluorescence on Ar number density. While laser action has not yet been observed for either F_2^* (Ar_2 F*) or Cl_2^*, both have large emission bandwidths of 5-60 nm, and they feature fluorescence efficiencies (photons/Argon metastable) 2-3 times that of Ar-N_2 mixtures at similar pressures. Thus, electron-beam excited mixtures of Ar/F_2 and Ar/Cl_2 are attractive sources of broadband incoherent UV radiation for photochemistry applications.

References

1. I_2: J. J. Ewing and C. A. Brau, Appl. Phys. Lett. 27, 557 (1975); M. V. McCusker, R. M. Hill, D. L. Huestis, D. C. Lorents, R. A. Gutcheck and H. H. Nakano, Appl. Phys. Lett. 27, 363 (1975).

2. Br_2: J. Murray, J. C. Swingle and C. E. Turner, Jr., Appl. Phys. Lett. 28, 530 (1976).

3. J. J. Ewing, J. H. Jacob, J. A. Mangano and H. A. Brown, Appl. Phys. Lett. 28, 656 (1976).

4. C. H. Chen and M. G. Payne, Appl. Phys. Lett. 28, 219 (1976).

5. R. K. Asundi and P. Ventkateswartu, Ind. J. Phys. 21, 101 (1947).

6. R. K. Stevnenberg and R. C. Vogel, J. Am. Chem. Soc. 78, 901 (1956).

7. M. Bodenstein and H. Jockusch, Z. Anorg. Allg. Chem. Dtsch. 231, 24 (1937).

8. H. von Wartenberg, G. Sprenger and J. Yaylor, Bodenstein-Festband, Ourrages, 61 (1931).

9. P. J. Hay and D. C. Cartwright, Chem. Phys. Lett. 41, 80 (1976).

10. D. C. Lorents, R. M. Hill, D. L. Huestis, M. V. McCusker, and H. H. Nakano, 3rd Colloquium on Electronic Transition Lasers, Aspen, Colorado; September, 1976.

1.3 Observation of Stimulated Emission in KrCl

Recent investigations[1-3] have verified the existence of a unique class of molecules, the rare-gas halides, that are capable of producing efficient lasing in the ultraviolet. To date, five members of this family (XeF, XeCl, XeBr, KrF, and ArF) have exhibited stimulated emission.[4]

In this paper, we report the observation of lasing in the KrCl complex at 222.9 nm utilizing electron-beam excitation of $Ar/Kr/Cl_2$ gas mixtures.

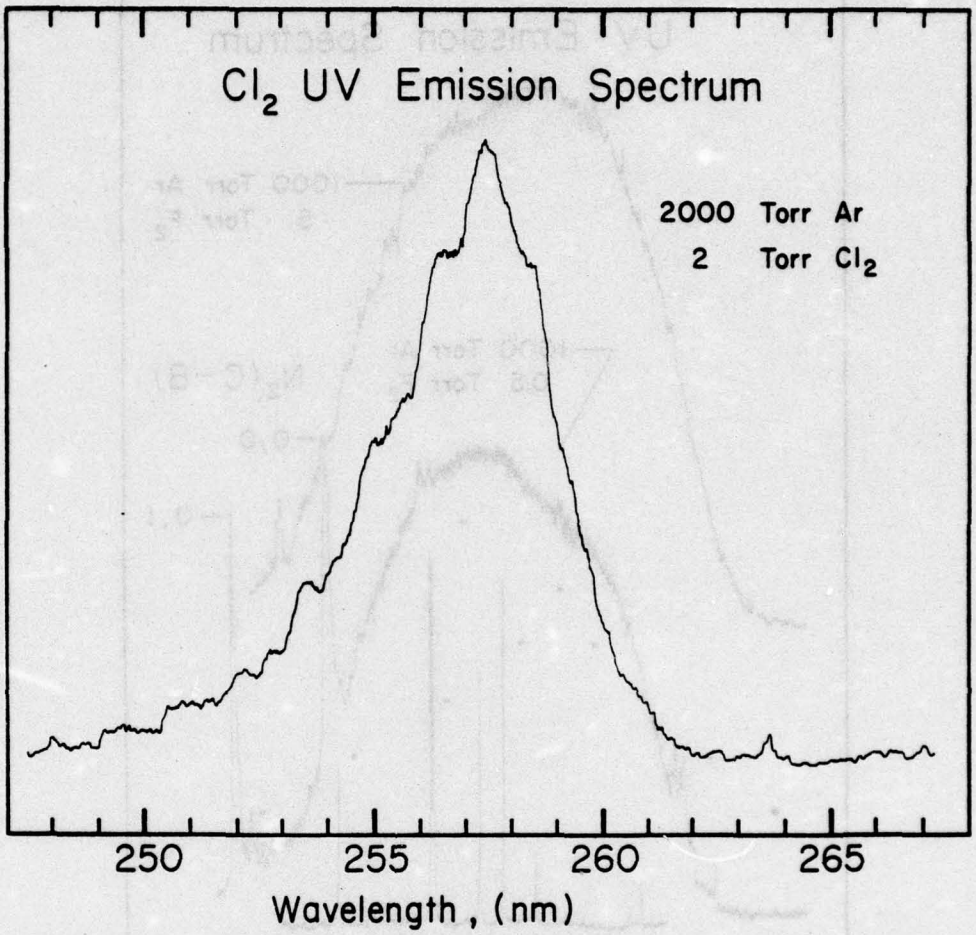

Fig. 21 — Emission spectrum of Cl_2 showing two overlapping vibrational series. The detection system resolution is ~ 0.3 nm

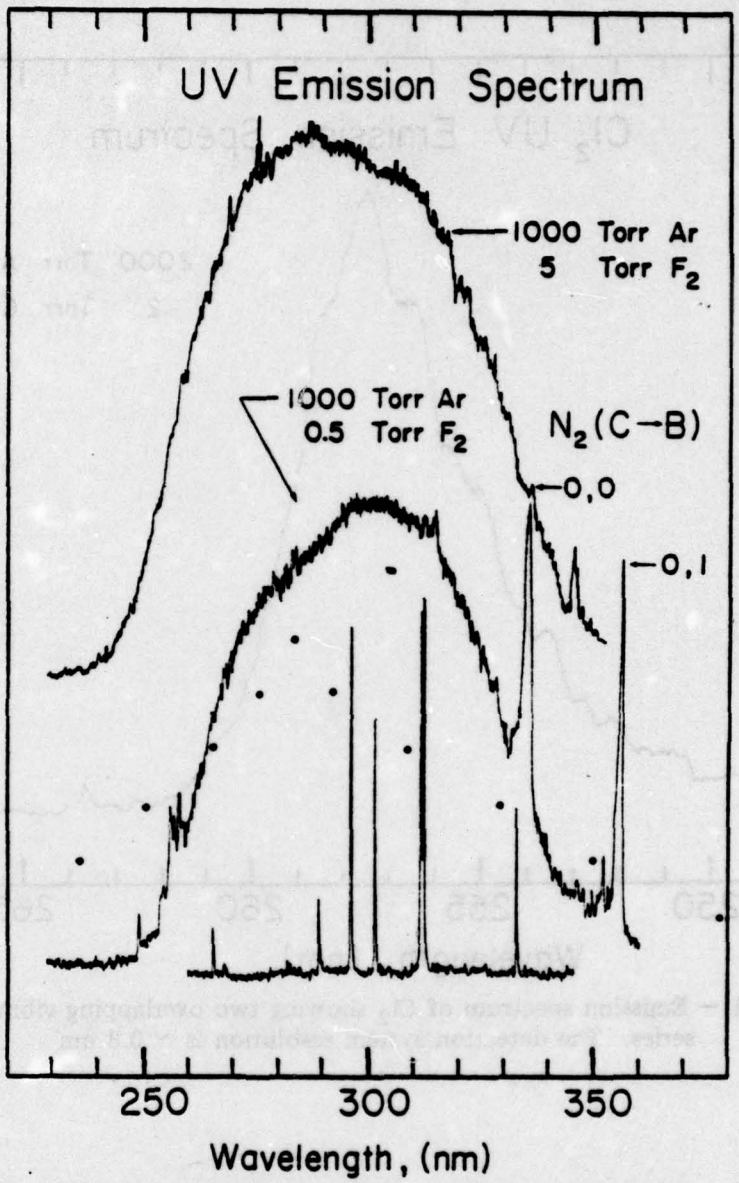

Fig. 22 — Ultraviolet emission spectrum obtained from e-beam excited Ar/F_2 mixtures. The F_2 absorption spectrum is indicated by the black dots. The $N_2(C \rightarrow B)$ 0.0 and 0.1 lines and the UV mercury spectrum are shown for wavelength calibration.

Both the laser cell and Inconel e-beam window foil were sprayed with Aerodag carbon spray to minimize loss of chlorine through chemical reaction with the cell walls. Solar blind or S-5 photodiodes were used in conjunction with neutral density filters calibrated to 200 nm to estimate laser power. Optical-quality sapphire flats were aligned normal to the laser cell's axis to reduce window reflection losses. The optical cavity initially consisted of two dielectric-coated mirrors ($R \gtrsim 99\%$) of 1-m radius of curvature that were separated by 30 cm. Subsequently, one mirror was replaced by an aluminum reflector ($R \sim 86\%$). Strong lasing, as evidenced by temporal and frequency narrowing of the spontaneous emission pulses, was observed in both cases.

Excitation of various $Ar/Kr/Cl_2$ mixtures revealed intense KrCl* and Cl_2^* emission (the asterisk denotes an electronically excited state). The spontaneous and laser emission spectra of KrCl* are shown in Fig. 23 for a gas composition of 3000 Torr Ar/200 Torr Kr/5 Torr Cl_2 which was found to yield maximum laser power output. The spontaneous emission spectrum was obtained by simply removing one mirror of the optical cavity.

Clearly, peak fluorescence occurs at ~ 222.5 nm in contrast to the laser wavelength of 222.9 ± 0.1 nm, indicating the possibility of ground-state absorption loss for

$\lambda \lesssim 222.8$ nm. Alternatively, KrCl* may be lasing on a single vibrational level (i.e., $v = 0$), whereas the spontaneous emission spectrum includes $v = 0, 1, 2, \ldots$ contributions. If this is the case, the ratio of spontaneous emission FWHM (~ 1.5 nm) to the laser linewidth (~ 0.5 nm) suggests that the KrCl* laser may be tunable over ~ 15 Å in a high-gain pumping scheme such as a transverse discharge.[6] Note also that the spontaneous emission profile exhibits oscillatory structure similar to that observed previously for other rare-gas-halide molecules. From the densitometer trace, the vibrational spacing of the KrCl electronic state responsible for lasing was estimated to be ~ 279 cm^{-1}, which is to be compared with $\omega_e \gtrsim 253$ cm^{-1} and 233 cm^{-1} obtained by Sommermeyer[7] and Clouser and Gordy,[8] respectively, for ground-state RbCl, the alkali-halide analog to KrCl*.

Golde[9] has interpreted the undulations of the low-pressure ($0.5 \leq p_{total} \leq 5$ Torr) spectrum of KrCl* as due to the overlap of the wave functions of the dissociative ground state and a vibrationally excited bound upper level. This analysis is certainly valid for low-pressure mixtures where the vibrational manifold is unrelaxed. That is, a newly formed KrCl* molecule will be vibrationally excited due to the exothermicity of the reaction

$$Kr^* + Cl_2 \rightarrow KrCl^* + Cl,$$

and is likely to radiate spontaneously before it can be

vibrationally deactivated by collisions with the background gas. However, at the high gas pressures encountered in this experiment (~ 4 atm), the KrCl* vibrational population rapidly collapses into the lowest one or two vibrational states (since ω_e ~ 280 cm^{-1} and kT ≃ 200 cm^{-1}). Thus, the emission spectrum directly reflects the vibrational spacing of the excited complex.[10] Therefore, Golde observed KrCl* emission intensity undulations of 1760 cm^{-1} (which were analyzed to yield a vibrational spacing ω_e of 208 cm^{-1}) as opposed to the 279-cm^{-1} oscillations reported here.

However, due to the dissociative KrCl ground state, the periodicity of the emission intensity undulations at high pressure slightly exceeds the true vibrational spacing of the exciplex. This explains our result for KrCl and those of Brau and Ewing[11] for XeBr and KrF.

Finally, the peak KrCl* emission wavelength of 222 nm is also in agreement with the 219-nm value predicted by the alkali-halide (RbCl) model.[3] Golde observed peak KrCl* fluorescence at low pressure to be at ~ 220 nm which may also be attributed to an unrelaxed vibrational manifold.[11]

Laser output power as a function of the partial pressure of the three constituent gases was studied. Lasing action was most critically dependent on the Cl_2 pressure; for example, lasing could not be achieved for 3000/200/10 Torr Ar/Kr/Cl_2 mixtures which is in agreement with the

results of Brau and Ewing[4b] for XeCl. Rapid quenching of KrCl* by Cl_2 is believed to be responsible for this behavior. Similarly, 3000 Torr of argon produced the best results; the output power at 2500 Torr (p_{Kr}, p_{Cl_2} fixed) dropped by a factor of 4 and laser action ceased at 3500 Torr. Competition of Cl_2^* formation, $Ar^M + 2Ar \rightarrow Ar_2^M$; $Ar_2^M + Cl_2 \rightarrow Cl_2^*$, with the Ar^M, $Ar_2^M \rightarrow Kr^M$ (M denotes a metastable species) energy transfer processes is likely to be an increasingly significant loss channel at higher argon pressures[12] and, in addition to deexcitation of KrCl* by Ar, will eventually terminate lasing, as seen experimentally. The dependence of the laser output on the partial pressure of krypton (shown in Fig. 24) reveals a dramatic decrease in power above ~ 225 Torr Kr which also is presumed to be due to quenching of KrCl* molecules by Kr.

The time-resolved KrCl* spontaneous emission and laser waveforms are shown in Fig. 25. The KrCl* fluorescence signal closely followed the e-beam current pulse ($\tau = 0$ corresponds to the initiation of the beam current). Approximately 30 ns is required for the laser to reach threshold.

As mentioned previously, two sets of mirrors have been used. Initially, two high-reflectivity ($R \geq 99\%$ at 223 nm) dielectric mirrors were installed giving 3.5-4.0 kW peak power output/mirror. Subsequently, one mirror was replaced by an aluminum-coated ($R \sim 86\%$) reflector. Although the

aluminum coating's opacity precluded a direct measurement of the power coupled out of the optical cavity, an estimate of 50 kW, based on an assumed 1% transmission for the dielectric and aluminum mirrors, was obtained. Since the mirrors used in these experiments actually transmitted < 1% (due to scattering and absorption losses in the coating), the 50-kW estimate is pessimistic. Therefore, we feel that much larger energies can be extracted from KrCl through the use of better mirrors (i.e., reduce coating losses to < 1%).

These results surpass the energies obtainable from the XeCl laser. Ewing and Brau[4b] obtained 3 kW of power at 308 nm in ~ 30 ns pulse ($Ar/Xe/Cl_2$ mixtures) and recently, Tellinghuisen and co-workers reported[13] 15 kW utilizing a larger e-beam device and $Ar/Xe/CH_2Cl_2$ or Cl_2 mixtures.

Moreover, absorption of KrCl* 223-nm photons by Cl_2 is negligible (< 0.1%/20 cm).[14] However, the KrCl laser power outputs produced in our experiments are an order of magnitude lower than those of KrF (248 nm) for excitation schemes and $Ar/Kr/F_2$ gas mixtures similar to those used for KrCl. Detailed kinetics calculations for e-beam-excited $Ar/Kr/Cl_2$ mixtures suggest[12] that the maximum theoretical efficiency of the KrCl laser is ~ 5-10%. Therefore, although KrCl appears to be of great interest, its ability

to compete with KrF and XeF as an efficient powerful source of uv radiation depends on the importance of loss processes such as photoionization and KrCl* quenching by Kr, Ar, and Cl_2.

In summary, 50 kW of KrCl laser power has been obtained from e-beam-pumped $Ar/Kr/Cl_2$ mixtures in a 30-ns FWHM pulse at 222.9 nm. (J. R. Murray and H. T. Powell have also recently observed lasing in KrCl Appl. Phys. Lett. 29, 252 (1976)). The laser emission wavelength and power output appear to be ideally suited for photochemical research and laser isotope separation studies, in particular.

References

1. M. F. Golde and B. A. Thrush, Chem. Phys. Lett. 29, 486 (1974).

2. J. E. Velazco and D. W. Setser, J. Chem. Phys. 62, 1990 (1975).

3. J. J. Ewing and C. A. Brau, Phys. Rev. A 12, 129 (1975).

4. (a) XeF: C. A. Brau and J. J. Ewing, Appl. Phys. Lett. 27, 435 (1975). (b) XeCl: J. J. Ewing and C. A. Brau, Appl. Phys. Lett. 27, 350 (1975). (c) XeBr: S. K. Searles and G. A. Hart, Appl. Phys. Lett. 27, 243 (1975). (d) KrF: E. R. Ault, R. S. Bradford, Jr., and M. L. Bhaumik, Appl. Phys. Lett. 27, 413 (1975). (e) ArF: J. M. Hoffman, A. K. Hays, and G. C. Tisone, Appl. Phys. Lett. 28, 538 (1976).

5. S. K. Searles and G. A. Hart, Appl. Phys. Lett. 28, 384 (1976).

6. The KrF laser has recently been tuned, in a transverse discharge device, over a 15-Å region centered at 2486 Å; R. Burnham (private communication).

7. K. Sommermeyer, Z. Phys. 56, 548 (1929).

8. P. L. Clouser and W. Gordy, Phys. Rev. 134, A863 (1964).

9. M. F. Golde, J. Mol. Spectrosc. 58, 261 (1975).

10. The wave-function overlap integral for the first two vibrational states of RX* (R and X are rare-gas and halogen atoms, respectively) with the RX ground state also provides a possible explanation for the appearance of a double peak in the "main continuum" emission spectra of several RX complexes at high pressure. The asymmetric character of the RX* potential well causes a fraction of the $\nu = 1$ emission to appear as a "hump" to the red side of the peak $\nu = 0$ emission. Accordingly, double-line laser emission has been obtained in KrF and ArF. Also, in our studies of KrF* spontaneous emission, the double peak was absent at low gas pressures (100 Torr Kr, 1 Torr F_2) due to smoothing of the spectrum by wave-function contributions from higher ($\nu > 2$) KrF* vibrational levels.

11. C. A. Brau and J. J. Ewing, J. Chem. Phys. 63, 4640 (1975).

12. J. G. Eden and S. K. Searles (unpublished).

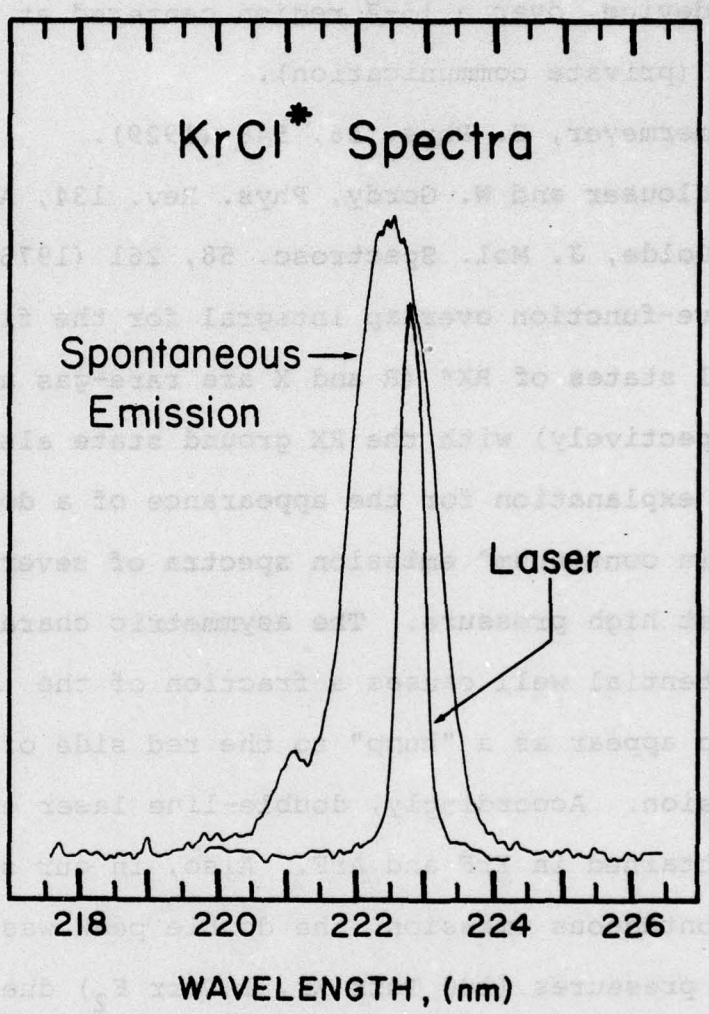

Fig. 23 — Laser and spontaneous emission spectra of KrCl* for 3000 Torr Ar, 200 Torr Kr, and 5 Torr Cl_2. The spectra were recorded on Kodak VUV 10 1-01 film and displayed using a Joyce-Loebl microdensitometer. Resolution of the detection system was 0.3 nm.

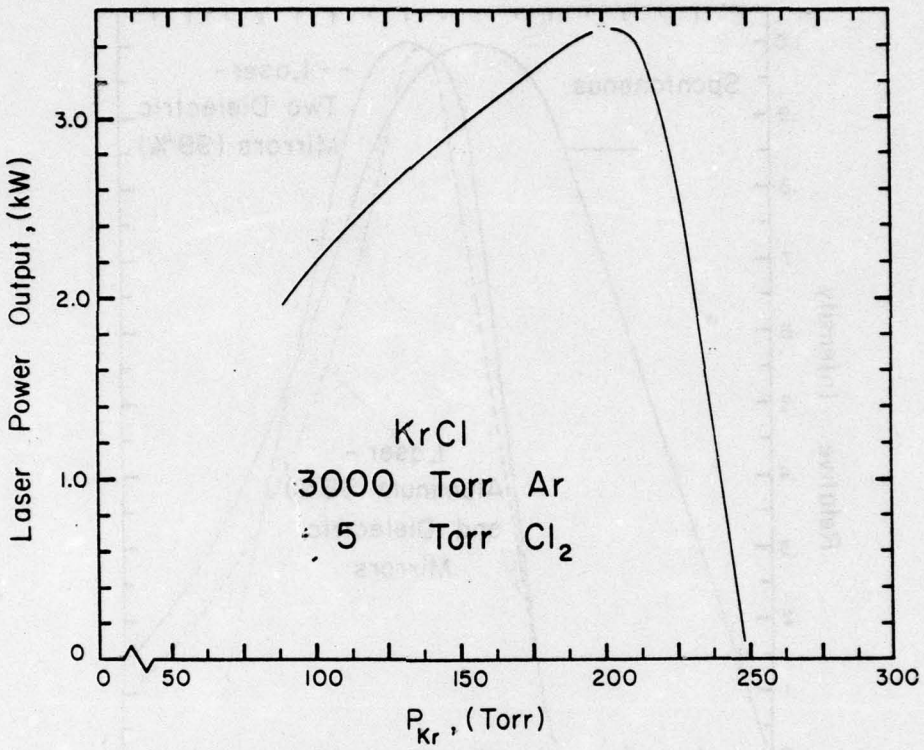

Fig. 24 — Variation of KrCl output power/mirror with the partial pressure of Kr in 3000 Torr Ar/Kr/5 Torr Cl_2 mixtures. Data were taken using high-reflectivity (R ~ 99%) mirrors.

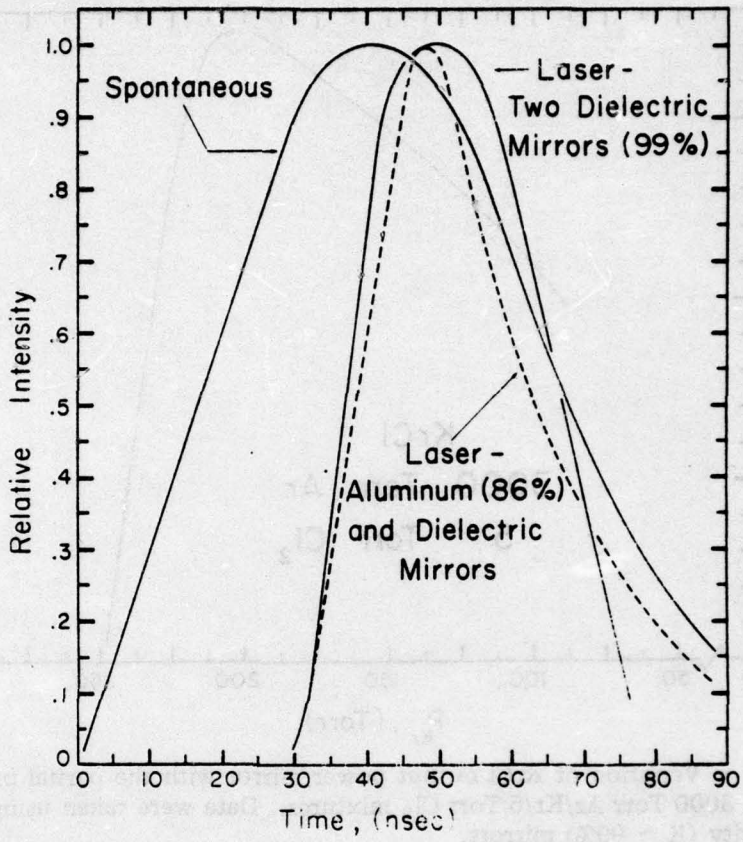

Fig. 25 — Spontaneous and laser emission waveforms. t=0 corresponds to initiation of the electron-beam current. The laser profiles represent optical cavity output couplings (estimated) of 1% (solid line) and 14% (dashed line).

13. J. Tellinghuisen, J. M. Hoffman, G. C. Tisone, and A. K. Hays, J. Chem. Phys. 64, 2484 (1976).

14. D. J. Seery and D. Britton, J. Phys. Chem. 68, 2263 (1964).

1.4 Kinetic Modelling of the KrCl Laser

To determine the feasibility of scaling the newly-discovered KrCl exciplex laser to higher powers and efficiencies, a simple kinetic model of $Ar/Kr/Cl_2$ gas mixtures has been constructed. This model assumes that since argon comprises > 90% of the laser gas mixtures, then the bulk of the absorbed electron energy results in the production of Ar (^3P) excited states. Through collisions of Ar (^3P) with the Ar, Kr, and Cl_2 gases, the atomic metastable energy is channeled to various products including $Cl_2^*(E)$, $ArCl^*(C\frac{1}{2})$, Cl_2^+, and $KrCl^*(C\frac{1}{2})$. Predictions of the model have been complemented by experimental measurements of the $Cl_2^*(E)$ and KrCl* spontaneous emission spectra for several $Ar/Kr/Cl_2$ gas mixtures. Briefly, the most important results of this investigation were: 1) the efficiency of the KrCl* laser was found to be ultimately limited by the efficiency for producing Kr* (^3P) excited states through Ar*, Ar_2^* + Kr collisions; 2) the branching ratio for the formation of $KrCl^*(C\frac{1}{2})$ from the reaction

$$Kr^* (^3P) + Cl_2 \rightarrow KrCl^*(C\tfrac{1}{2}) + Cl \qquad (1)$$

is 0.9 $\pm$ 0.1, and 3) quenching of KrCl* molecules by Cl_2 proceeds at a rate of $< 3 \cdot 10^{-11}$ cm^3 - sec^{-1}.

These results strongly suggest that KrCl is attractive as an efficient (η_{max} ~ 5-10%) scalable source of stimulated emission in the ultraviolet.

The details of the KrCl kinetic model and its conclusions will be discussed in an NRL memorandum to be published.

2. Rare Gas Halide Laser Parameters

In the rare gas halide laser area, our efforts have been directed towards the measurement of crucial kinetic parameters during this reporting period. The self-sustained discharge excited rare gas halide laser developed at NRL is particularly well suited for this purpose because of its ease of operation. Although some of the results obtained to date are still preliminary in nature, the validity of the approach used is now well established. These results were reported at the IXth International Conference on Quantum Electronics held near the end of this reporting period.

Information about quenching rates and saturation intensity in the laser medium was obtained by monitoring the laser level densities, under zero-field and saturated conditions, and the corresponding intracavity flux. For the KrF system, this technique only requires the measurement of zero-field and saturated side fluorescence together with

the laser output. For XeF, due to the presence of a bound lower laser level, simultaneous zero-field and saturated gain measurements also need to be made.

Since the lower level for the KrF laser is dissociative, the rate equations for the upper level density under zero-field and saturated conditions are simply

$$\frac{d\, N_u^o}{dt} = P_u - \gamma_u N_u^o \qquad (1)$$

$$\frac{dN_u}{dt} = P_u - \gamma_u N_u - \frac{\sigma I}{h\nu} N_u \qquad (2)$$

where N_u^o is the zero-field upper state density, N_u is the saturated upper state density, P_u represents the pumping of the upper state, γ_u is the quenching rate, σ the stimulated emission cross section, I the intracavity laser intensity, and $h\nu$ the energy of the laser photon. Combining and rearranging Eqs. (1) and (2) gives

$$\frac{\frac{d}{dt}\,(N_u^o - N_u)}{\gamma_u\,(N_u - N_u^o) + \frac{\sigma I}{h\nu} N_u} = 1 \qquad (3)$$

In this expression, the densities and their derivatives as well as the intensity, I, are measurable functions of time. One can thus make a two parameter fit to find γ_u and σ. Furthermore, since the densities appear in all terms in Eq. (3), they only have to be known on a relative basis.

This was readily accomplished by monitoring the fluorescence from the side of the laser cell.

A typical set of results showing the dependence of the zero-field and saturated side fluorescence and the laser output is given in Fig. 26. All the traces were triggered in the same manner so a direct comparison among them could be made. The decrease in upper state density as the laser field builds up is clearly visible in these traces. The intracavity flux required in the analysis can be calculated from the output intensity and the mirror transmissivity. The combination of γ_u and σ which, when used to form the ratio in Eq. (3), gives the least deviation from unity for all times is

$$\gamma_u = 2 \times 10^8 \text{ sec}^{-1}$$

and $$\sigma = 7 \times 10^{-17} \text{ cm}^2.$$

Using the measured bandwidth of 2 nm for the KrF laser transition, one calculates a radiative rate of

$$A = 0.3 \times 10^8 \text{ sec}^{-1}.$$

Comparing the values for A and γ_u, one sees that collisional quenching of the KrF upper laser level is by far the more important deactivation pathway.

It is interesting to note that so long as output transmission constitutes the major source of cavity loss, the laser energy extracted is related to the time integrated zero-field and saturated upper state densities as follows:

$$\text{Laser Energy/Area} = \frac{h\nu L}{2} \gamma_u (N_u^o - N_u)\, dt$$

where L is the active length of the laser medium. It is thus possible to determine the absolute upper state densities from the data in Fig. 26. For the particular case shown, the maximum of the zero-field fluorescence corresponds to an excited KrF density of 2.5×10^{14} cm^{-3}. One can further estimate the density of Kr*, assuming that Kr* + F_2 is the primary formation reaction for excited KrF. Using a reaction rate constant of $k = 5 \times 10^{-10}$ cm^{-3} sec^{-1} as measured by Setser, one obtains a metastable density of Kr* = 10^{15} cm^{-3} at the peak of the fluorescence. Such a large metastable density could cause appreciable attenuation of the laser field, as a result of photoionization and the extent of this absorption is a subject for further investigation. Other topics to be examined in greater detail will include the role of electrons and the laser gas composition in quenching excited KrF.

A similar experiment has been done for the XeF laser system. Because of the existence of a bound lower state in this case, additional quantities needed to be measured. The zero-field and saturated rate equations for the XeF laser level densities are

$$\frac{dN_u^o}{dt} = P_u - \gamma_u N_u^o \qquad (4)$$

$$\frac{dN_u}{dt} = P_u - \gamma_u N_u - (N_u - N_l)\frac{\sigma I}{h\nu} \quad (5)$$

$$\frac{dN_l^o}{dt} = P_l + \gamma N_u^o - \gamma_l N_l^o \quad (6)$$

$$\frac{dN_l}{dt} = P_l + \gamma N_u - \gamma_l N_l + (N_u - N_l)\frac{\sigma I}{h\nu} \quad (7)$$

where u and l denote upper and lower states, the superscript stands for zero-field and the absence of it for saturated densities. Here γ_u is the total quenching rate for the upper state, γ is the cascade rate from the upper to the lower state due to both radiative and collisional processes and γ_l is the quenching rate for the lower state. It should be noted that σ is the stimulated emission cross section averaged over all the emitting lines. One is justified in making use of this concept, since the entire XeF band system is homogeneously broadened under our operating conditions.

The analogous expression to Eq. (3) now becomes

$$\frac{\gamma_u(N_u - N_u^o) + \frac{d}{dt}(N_u - N_u^o)}{\gamma(N_u - N_u^o) - \gamma_l(N_l - N_l^o) - \frac{d}{dt}(N_l - N_l^o)} = 1 \quad (8)$$

Note that the term involving σI has been eliminated but two additional quenching rates have appeared. More difficult experimentally, however, is the fact that now information must also be obtained on the lower laser level density.

One way of acquiring that information is through gain measurements on the laser transition under both zero-field and saturated conditions. This can be accomplished by taking advantage of the fact that the Ar ion laser line at 351.1 nm overlaps the XeF central laser band (see Fig. 27) and thus can be used as a convenient probe source for the gain measurements. Since the XeF bands are homogeneously broadened, no precise knowledge of the overlap is required.

A schematic for the XeF laser diagnostic experiment is shown in Fig. 28. Five separate quantities are measured in this experiment: the zero-field and saturated side fluorescence, zero-field and saturated gain, and the laser output. The argon ion laser probe beam was sent through the laser cell at a slight angle to the optical axis to avoid interference from the XeF laser beam. Low reflectivity mirrors were used for the XeF laser cavity so as not to excessively attenuate the probe beam. Movable stops were used near each end mirror which could spoil the laser cavity without blocking the probe beam. The laser output was monitored by both a photodiode for its temporal behavior and a pyroelectric detector for its energy content.

The results of the side fluorescence and gain measurements are given in Figs. 29 and 30. Due to the low Q of the cavity employed, the effect of laser oscillation on the spontaneous emission was small, although definitely discernable.

In comparison, the saturation of gain under identical conditions was much more pronounced. (The magnitude of the integrated gain at the peak was approximately 20.) One sees immediately from these data that significant lower level bottlenecking exists for the XeF laser system.

To interpret these results on a more quantitative basis, one must go back to the rate equations, but first normalizing the small signal gain data with respect to the spontaneous emission data, so that they can be used together in the overall analysis. The properly normalized results are shown in Fig. 31. Here N_u^o and N_u are the zero-field and saturated side fluorescence traces, while $N_u^o - N_l^o$ and $N_u - N_l$ are logarithms of the corresponding small signal gain traces. The diamond at the peak of the population difference curves shows the possible range of normalization based upon the following arguments. First, the $N_u^o - N_l^o$ curve must lie below the N_u^o curve at all times. This constraint would be violated at the points indicated by the two downward pointing arrows if the population difference curves exceeded the top of the diamond. To obtain a lower bound on the normalization, we examine the zero-field and saturated side fluorescence traces shown in Fig. 32 which have been obtained under the same conditions as earlier except with a higher Q cavity. We make use of the fact that at any point in time the saturated upper state density must

be greater than the saturated lower state density which in turn must be greater than the zero-field lower state density. Therefore, the zero-field population difference must be at least as large as the difference between the zero-field and saturated upper state densities at any time. Applying these arguments at the point of maximum saturation (t = 60 nsec), we obtain a lower bound for $N_u^o - N_l^o$ as indicated by the tip of the upward pointing arrow in Fig. 31. For the peak of $N_u^o - N_l^o$, this lower bound corresponds to the bottom of the diamond. The actual population difference curves as drawn were taken halfway between the upper and lower bounds.

An attempt was made to find γ_u, γ, and γ_l using the curves in Fig. 31 together with Eq. (8), but proved to be unfeasible. However, we note that for t > 50 nsec both $N_u^o - N_u$ and $N_l^o - N_l$ are approximately constant. It is then possible to neglect the derivative terms in Eq. (8) and obtain the following expression:

$$\gamma_u = \gamma + 4\,\gamma_l. \tag{9}$$

Since γ must be positive, we have

$$\gamma_l < 0.25\,\gamma_u \tag{10}$$

Additional relations may be obtained from the application of Eq. (6) at the peak of the population curves where $\frac{dN_l^o}{dt} = 0$. Since P_l must be positive, it follows that

$\gamma_1 N_1^o > \gamma N_u^o$ at that point. For the curves in Fig. 31, this leads to

$$\frac{\gamma_1}{\gamma} > 2.7 \qquad (11)$$

Substitution of this into Eq. (9) gives

$$\gamma_1 > 0.23\ \gamma_u \qquad (12)$$

and

$$\gamma < 0.09\ \gamma_u . \qquad (13)$$

Note that inequalities (10) and (12) give us a well bounded ratio between γ_1 and γ_u. Finally, the results of Fig. 31 together with the measured laser output can be put into Eqs. (4) and (5) to give:

$$\gamma_u = 1.5 \times 10^8\ \text{sec}^{-1}$$

$$\sigma = 3 \times 10^{-17}\ \text{cm}^2$$

Using the above value for γ_u in Eqs. (10), (12), and (13) leads to

$$\gamma_1 = 0.36 \times 10^8\ \text{sec}^{-1}$$

and

$$\gamma < 0.13 \times 10^8\ \text{sec}^{-1}.$$

The conclusions from these studies are that CW laser action in XeF should be possible (since $\gamma_1 > \gamma$) but such a laser would not be very efficient (since $\gamma_1 << \gamma_u$). The long pulse XeF laser experiments performed on NRL's Maxwell device have confirmed the first prediction and seem to support the second. To improve upon the efficiency of the long pulse XeF laser, one would have to find means to preferentially quench the lower level. One possible solution could be to operate the laser at an elevated temperature.

KrF SIDE FLUORESCENCE

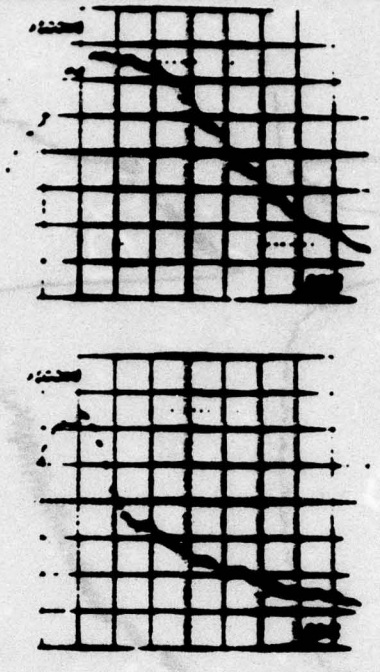

KrF LASER PULSE

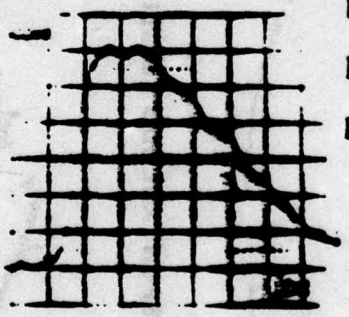

Fig. 26 — Side fluorescence from KrF upper laser level in the absence and presence of a cavity, and accompanying laser pulse

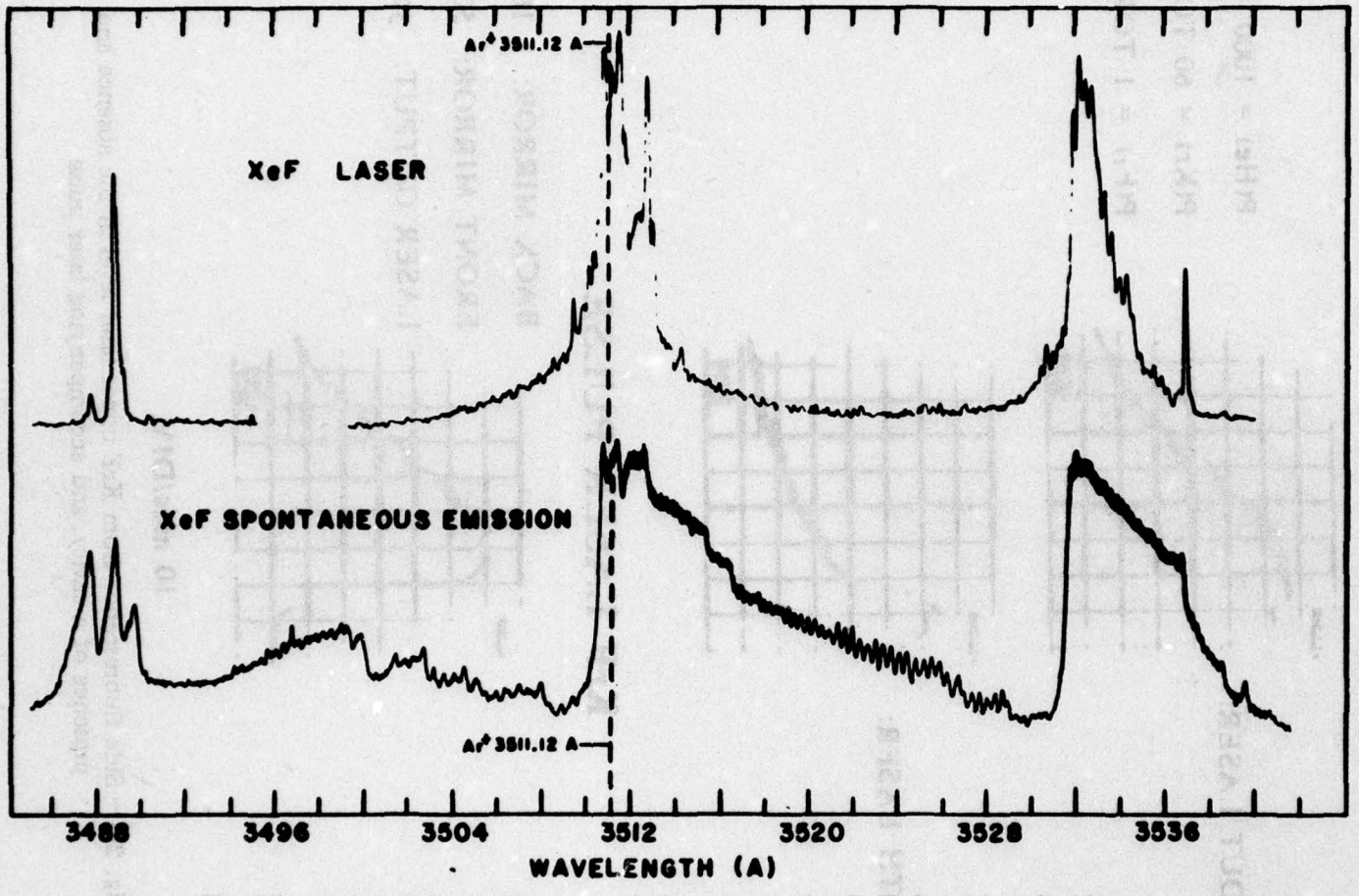

Fig. 27 — Laser and spontaneous emission spectra for XeF showing coincidence with the 3511.12 Å line of the Ar ion laser

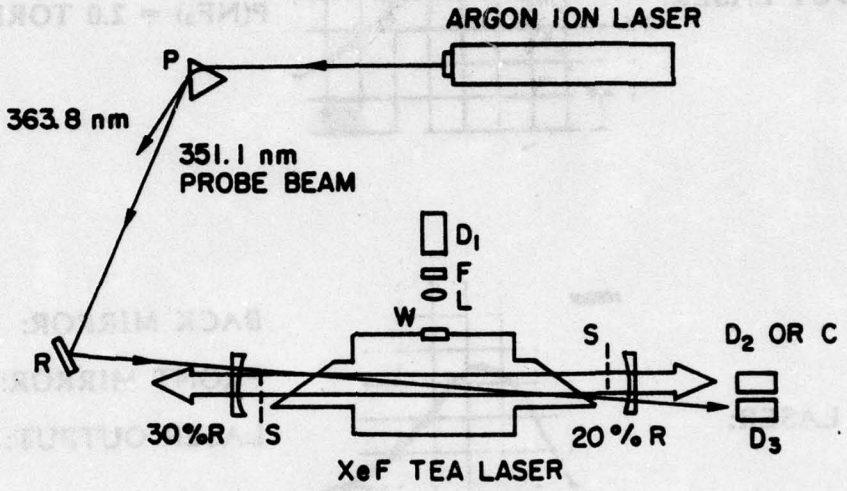

Fig. 28 — Schematic for gain and side fluorescence measurements on the XeF laser

XeF SIDE FLUORESCENCE

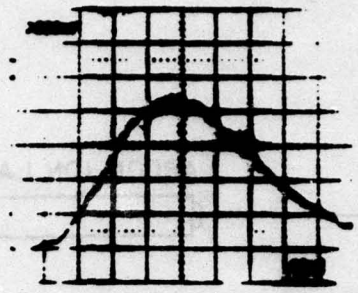

WITHOUT LASER:

P(He) = 1000 TORR

P(Xe) = 2.5 TORR

$P(NF_3)$ = 2.0 TORR

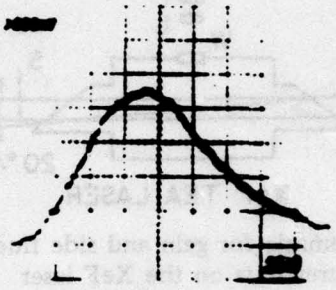

WITH LASER:

BACK MIRROR: 30% R

FRONT MIRROR: 20% R

LASER OUTPUT: 5 mJ

10 nsec/DIV.

Fig. 29 — Side fluorescence from XeF upper laser level in the absence and presence of a cavity

XeF GAIN MEASUREMENTS

P(He) = 1000 TORR

P(Xe) = 2.5 TORR

$P(NF_3)$ = 2.0 TORR

WITHOUT LASER:

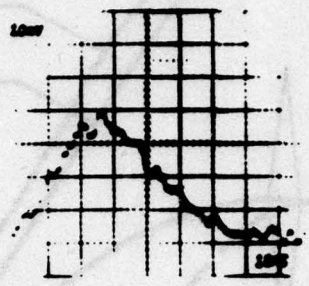

BACK MIRROR: 30% R

FRONT MIRROR: 20% R

LASER OUTPUT: 5 mJ

WITH LASER:

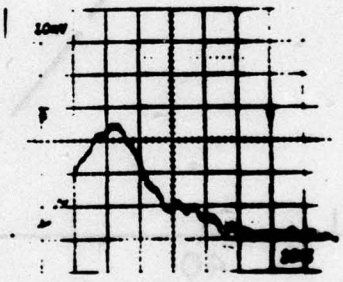

10 nsec/DIV.

Fig. 30 — Integrated small signal gain for zero-field and saturated XeF laser amplifier

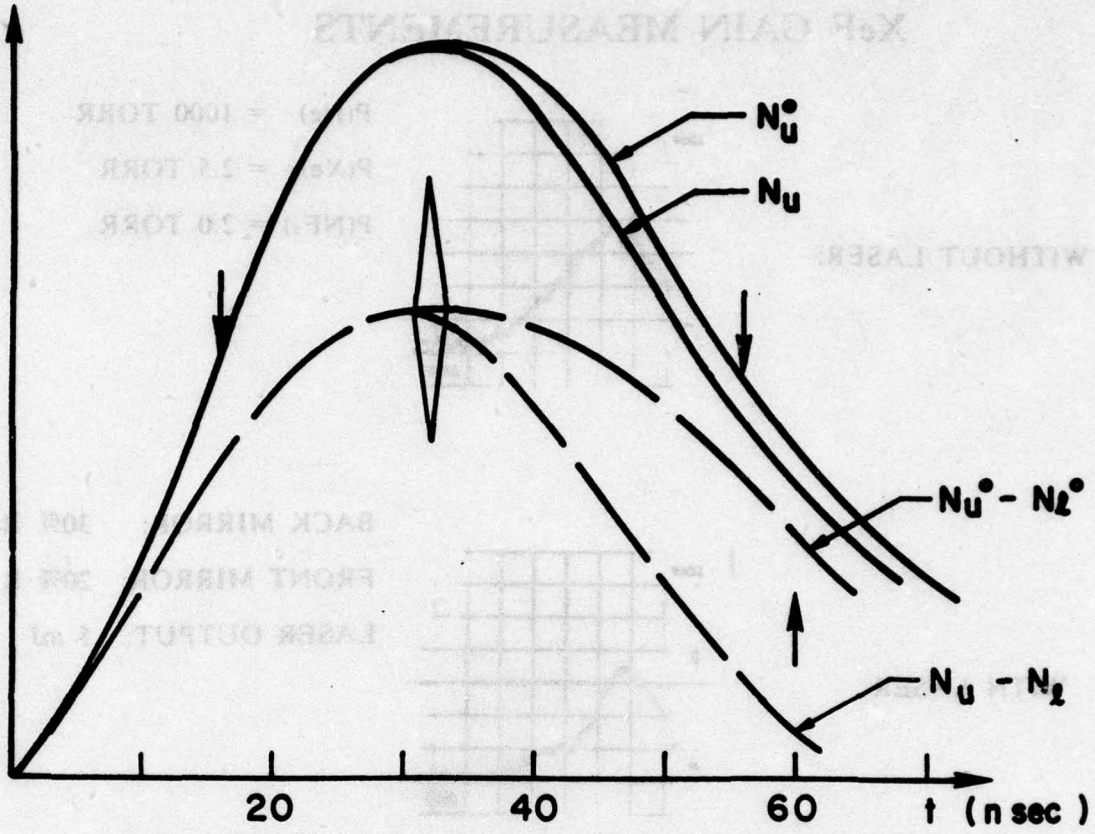

Fig. 31 — Temporal behavior of the upper state and population difference densities in XeF under zero-field and saturated conditions

XeF SIDE FLUORESCENCE

(LOW LOSS CAVITY)

P(He)	= 1000 TORR	BACK MIRROR:	100% R
P(Xe)	= 2.5 TORR	FRONT MIRROR:	70% R
$P(NF_3)$	= 2.0 TORR	LASER OUTPUT:	20 mJ

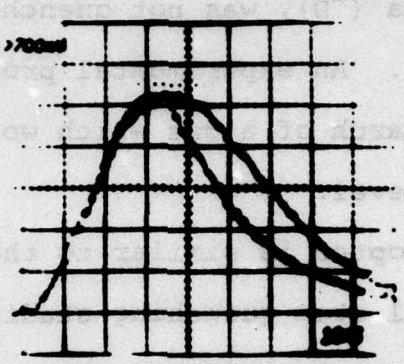

Fig. 32 — Side fluorescence from XeF upper laser level for zero-field and highly saturated conditions

3. Chemical BaO-Ba Transfer Laser Studies

During the last reporting period, it was established through spontaneous emission measurements that sufficiently high Ba (^1P) densities are present in the Ba + N_2O flame for the purpose of achieving laser action on the Ba ($^1P \rightarrow {}^1D$) transition. However, direct gain measurements showed that population inversion did not exist in spite of the large Ba (^1P) concentration. The implication is that the lower laser level, Ba (^1D), was not quenched rapidly enough in these experiments. An experimental program was therefore initiated in search of a gas which would preferentially quench the Ba (^1D) level.

The approach adopted is similar to that used successfully for other metal atom quenching studies made at NRL. A short pulse dye laser is used to excite Ba atoms from the (^1S) ground state to the (^1P) state. The (^1D) state is populated by cascade radiative decay from (^1P), and its density is monitored by the absorption of a CW dye laser beam tuned to the wavelength of a strong transition terminating there. The recovery of that absorption following the excitation pulse would then yield directly the quenching rate for (^1D).

During this reporting period, an apparatus has been instrumented which will serve as the interaction chamber for the quenching experiment. A schematic for this flow

reactor is shown in Fig. 33. The bulk metal is placed in an alumina crucible which is heated by a tungsten filament. An inert gas is introduced below the crucible and travels upward to entrain the metal vapor and carry it into the interaction region. Known amounts of quenching gas can be mixed with the Ba vapor stream near the bottom of the reactor. In addition, three sets of windows are provided to permit an assessment of the extent of reactive quenching. This furnace is undergoing testing at present, and actual quenching studies will commence shortly.

4. Collisional Quenching of Electronic States

The cyclic metal vapor lasers have been predicted to be capable of extremely high efficiencies ~ 10%. Thus far, the best realized efficiency is about an order of magnitude lower. One possible reason for this discrepancy is that, although the electron impact excitation cross section for the metastable lower laser level is small, the net rate for that excitation could be quite substantial due to the preponderance of low energy electrons. This coupled with the lack of any deactivation mechanism for the metastable state then drastically reduces the laser efficiency.

Additional problems with existing cyclic lasers are the relatively short pulse length due to their self-terminating nature and the high optical gain which implies low energy storage capability. However, if self-quenching of

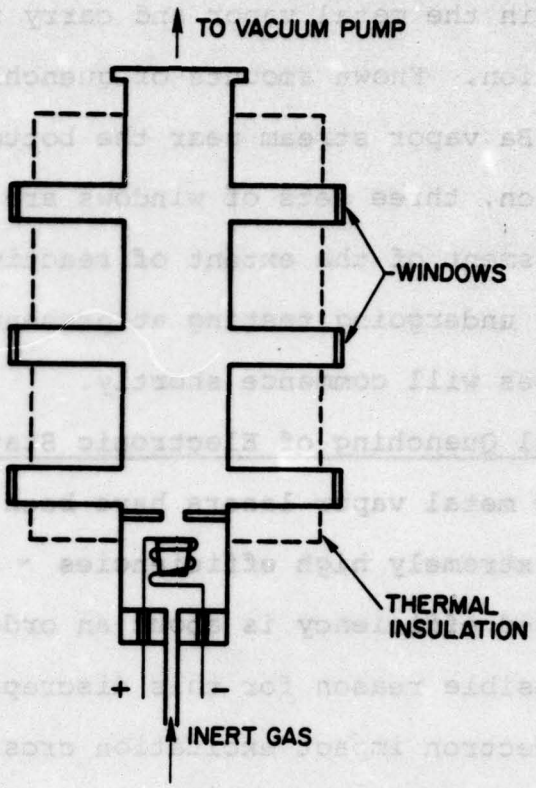

Fig. 33 — Schematic diagram of Ba furnace and flow apparatus

the metastable level is effective, one should be able to operate these lasers on a quasi-CW basis and with improved efficiency by going to high metal vapor pressures. The latter feature would lead to better energy storage properties through resonance broadening of the upper laser level. For these reasons, the self-quenching of the metastable Tl level has been studied as a prototype case.

A simplified atomic energy level diagram of Tl is shown in Fig. 34. Atoms initially in the ground state ($6\ ^2P_{1/2}$) are pumped to the upper laser level ($7\ ^2S$) by a dye laser tuned to 377.6 nm, and then radiate to the lower laser level ($6\ ^2P_{3/2}$) which is metastable. The population of the metastable level is monitored by absorption of radiation at 351.9 nm which is a transition from the ($6\ ^2P_{3/2}$) to a higher lying state. Figure 35 is a schematic illustration of the experimental ar angement. Thallium vapor is produced in a quartz cell by heating of the bulk metal. The quartz cell is designed so that the temperature of the Tl atoms in the upper part can be controlled independently of the number of Tl atoms (determined by the vapor pressure of the bulk metal in the lower part). A Tl microwave discharge lamp provides the probe radiation at 351.9 nm which is detected with a monochromator and photomultiplier tube. The probe lamp is operated continuously, and the dye laser is pulsed. Therefore, the time-dependence of the signal

shows large absorption immediately after the dye laser is fired, and a relatively slow decay due to collisional quenching. Figure 36 is a photograph of an oscilloscope trace showing this signal with a maximum absorption of about 60%. Absorption gradually decreases toward the right approaching nearly 100% transmission through the cell as the metastable population decays. This data may be reduced and graphed to determine the decay rate $\frac{1}{\tau}$ (where τ is the lifetime). In Fig. 37 three different decay rates (taken at different Tl vapor pressures) have been plotted. Ideally, the data points would lie along straight lines, and in general good agreement is shown. However, for short times the data points consistently roll off the straight line plot. The mechanism responsible for the roll off behavior is not understood fully at this time, but is of secondary importance since accurate values for $\frac{1}{\tau}$ can be obtained from the remaining data points. If the decay of the metastable atoms is due to collisional quenching by ground state atoms then the decay rate $(\frac{1}{\tau})$ should be proportional to the vapor pressure of ground state atoms and lead to the quenching rate and cross section. Unfortunately, the data obtained so far has been inconsistent with regard to the linearity of the decay rate with Tl vapor pressure, yielding different results at different times for the same vapor pressure. These difficulties have been traced to impurity effects in the quartz

Tl sample cell which have been discovered to be due to impurities in the thallium metal sample. Several sources of thallium were used that quoted high metal purity, but nevertheless had rather substantial amounts of halides present. At this time a method of purification is being developed, and once this is accomplished the experiments will be resumed.

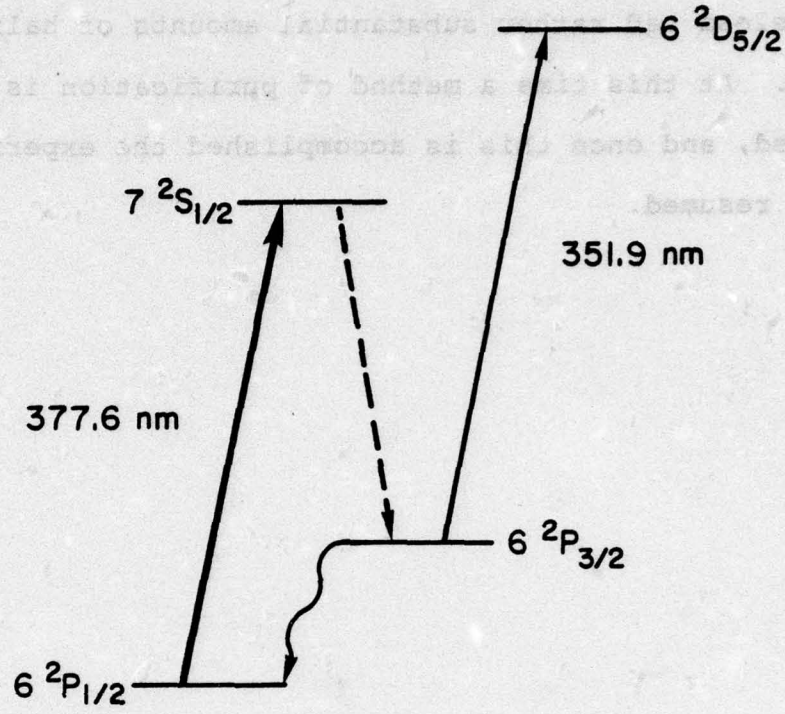

Fig. 34 — Energy levels involved in the measurement of T1 (6 $^2P_{3/2}$) level quenching

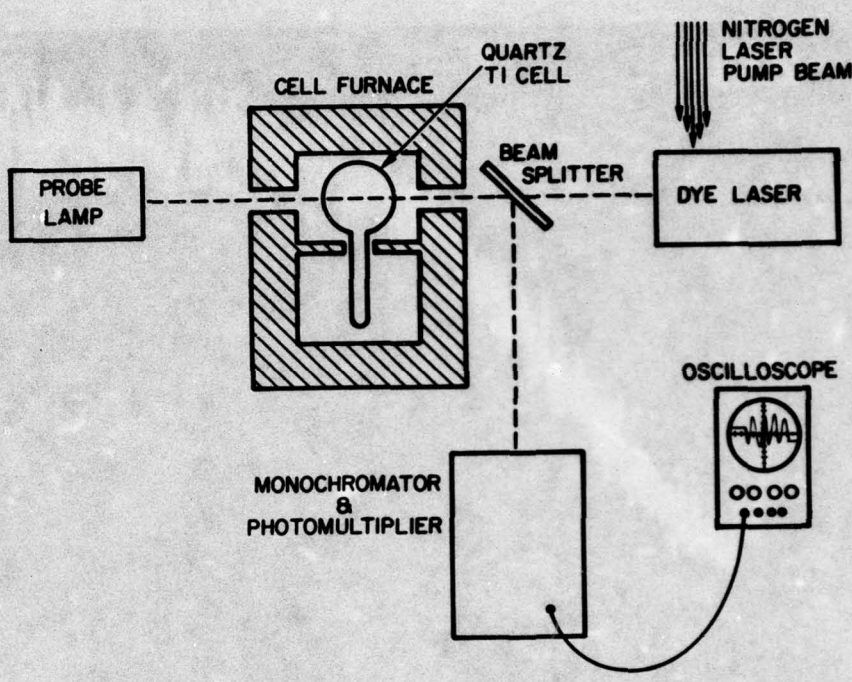

Fig. 35 — Diagram of T1 self-quenching experiment

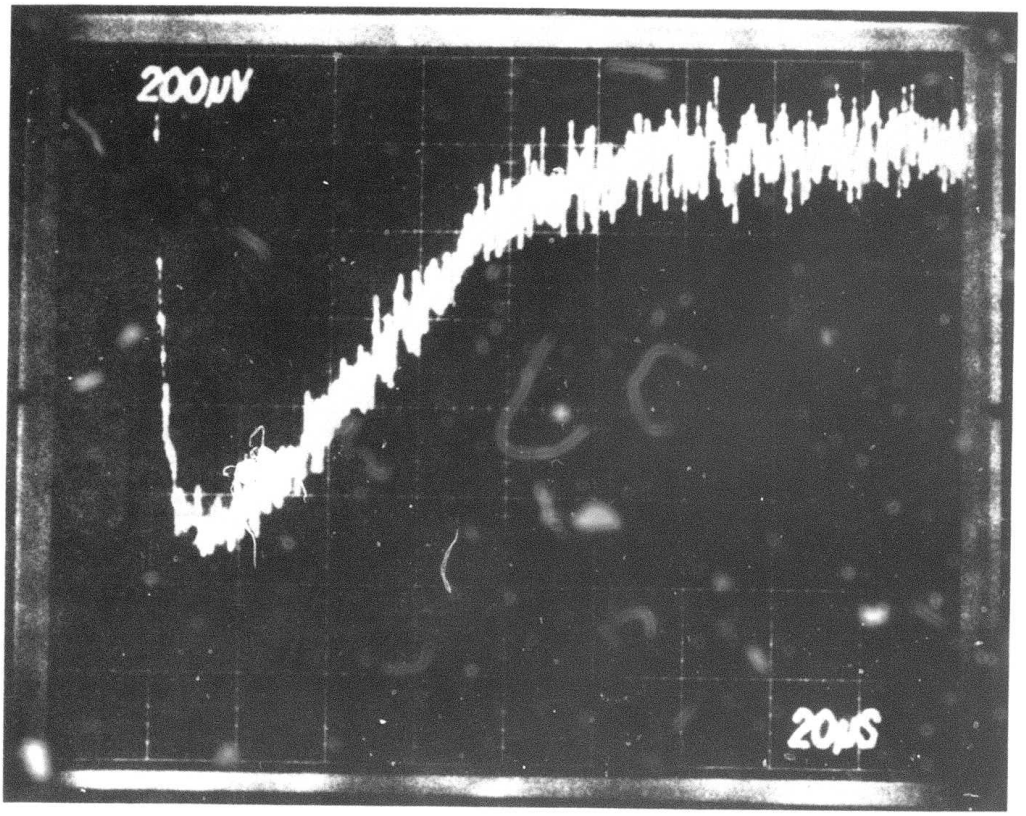

Fig. 36 -- Typical trace of transient absorption
of the 351.9 nm line in T1

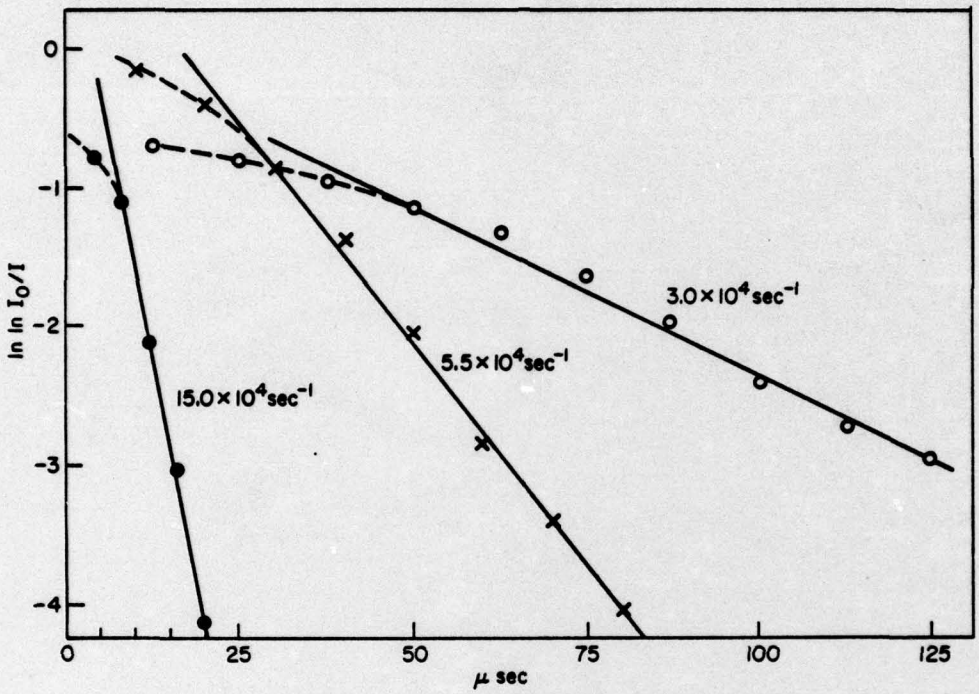

Fig. 37 — Plot of lnln (Io/I) for the 351.9 nm line as function of time for several T1 vapor pressures